

LHCb RICH 2 Engineering Design Review Report

Members of the LHCb RICH group

University of Bristol, Bristol, UK

N.Brook, J.Cole, R.Head, A.Phillips, A.Presland, F.Wilson

University of Cambridge, Cambridge, U.K.

A.Buckley, K.George, V.Gibson, C.Jones, S.G.Katvars, C.Shepherd-Themistocleous,
C.P.Ward, S.A.Wotton

CERN, Geneva, Switzerland

E.Albrecht, M.Benayoun, A.Braem, M.Campbell, C.D'Ambrosio, R.Forty, C.Frei, T.Gys,
M.Laub, J.Libby, M.Losasso, D.Piedigrossi, W.Snoeys, O.Ullaland, K.Wyllie

University of Edinburgh, Edinburgh, U.K.

A.Barczyk, R.Chamonal, S.Eisenhardt, A.Khan, J.Lawrence, F.Muheim, S.Playfer

University of Genova and INFN, Genova, Italy

M.Ameri, S.Cuneo, F.Fontanelli, V.Gracco, G.Mini, P.Musico, A.Petrolini, M.Sannino

University of Glasgow, Glasgow, U.K.

A.J.Flavell, A.A.Macgregor, V.O'Shea, C.J.Parkes, A.N.Pickford, F.J.P.Soler¹

Imperial College, London, U.K

L.Allebone, G.J.Barber, P.Dornan, A.Duane, U.Egede, M.Girone², R.Hill, S.Jolly, D.R.Price,
P.Savage, D.Websdale, R.White

University of Milano and INFN, Milano, Italy

T.Bellunato², M.Calvi, C.Matteuzzi, M.Musy, P.Negri, C.Piazzoni

University of Oxford, Oxford, U.K

M.Adinolfi, J.Bibby, G.Damerell, N.Harnew, C.Newby, J.Radermacker, N.Smale,
S.Topp-Jorgensen, G.Wilkinson

Rutherford Appleton Laboratory, Chilton, UK

C.A.J.Brew, C.J.Densham, S.Easo, B.Franek, J.G.V.Guy, J.A.Lidbury, J.V. Morris,
A.Papanestis, G.N.Patrick, S.A.Temple, M.L.Woodward.

¹ also at RAL

² presently at CERN

Abstract

The LHCb detector is a single arm spectrometer designed to exploit the large number of b-hadrons produced at the LHC in order to make precision studies of CP asymmetries and of rare decays in the B-meson system. It is therefore essential for the experiment that the detector configuration includes a particle identification system with high separation power between kaons and pions. We will present in this note the engineering solutions for the lightweight, high precision Ring Imaging Cherenkov detector, RICH 2, of the spectrometer. The design is built around a large space frame used as a high stability support for the optical system and as a supporting structure for the magnetic shielding needed for the photon detectors. All material not essential for the operation of the detector is located outside the acceptance of the spectrometer. The space frame also defines the Cherenkov gas volume.

1 Introduction

The LHCb experiment as shown in figure 1 is described in reference [1]. The particle identification system of the experiment includes two RICH detectors, RICH1 and RICH2. The basic requirement for this combined system is to provide particle identification over a wide momentum range, from 1 to ≥ 100 GeV/c. The technical design of the system is given in reference [2]. This note will describe the engineering choices taken for RICH2. The RICH2 is placed between $9450 \text{ mm} \leq z \leq 11900 \text{ mm}$. It covers the reduced angular acceptance of 120 mrad horizontally and 100 mrad vertically. It is placed between the last tracking station [3] at $z \leq 9415 \text{ mm}$, of the spectrometer and the first muon station [4] at $z \geq 11920 \text{ mm}$. The Cherenkov medium is CF_4 , $[n - 1] 10^6 = 0.1249 / [61.81^{-2} - \lambda^{-2}]$ at STP for λ in nm. It is operated at atmospheric pressure and at room temperature. To gain mechanical stability and to limit to the very minimum the material in the total acceptance range of the spectrometer, the detector does not split in two halves along the $x = 0$ plane. The detector is therefore placed and surveyed into position as one unit on the beam line. The vacuum chamber is then installed. The central acceptance of the detector is limited by a tube, the central tube as described in chapter 4, which runs coaxial to the vacuum chamber at a distance 45 mm from it. This distance is required in order to accommodate the heating jacket and the thermal insulation which is needed during the bake-out of the vacuum chamber.

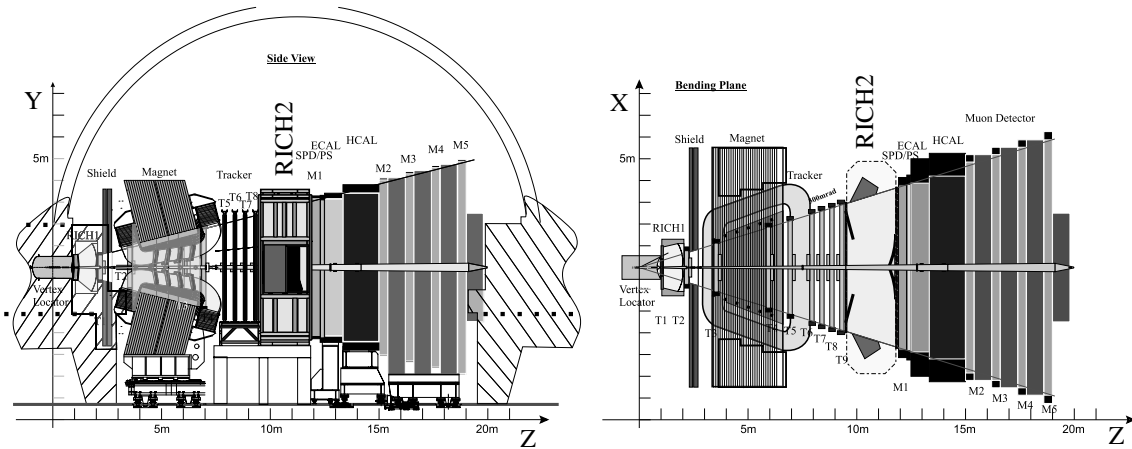


Figure 1: The LHCb experiment.

1.1 Changes from the RICH TDR

The basic design philosophy is unchanged from the RICH TDR, but with the broad understanding of the spectrometer and the implications of the choice of material and the interplay between the different subsystems of the detector, a number of adaptations have been made. We will list here the major changes.

- In the process of the optimisation of the spectrometer together with the mechanical and optical lay-out of the detector, chapter 2.3, the effective track length in the Cherenkov gas has been increased by about 20%.
- The superstructure, chapter 3, is made from closed aluminium profiles and not from stainless steel I profiles. The rigidity of the structure is maintained with a large reduction in weight. The skins of the entrance window is made from carbon fibre and the skins of the exit window from aluminium. The entrance window is also slightly smaller than in

the RICH TDR. The unavoidable radiation length introduced by the window structures is therefore moved closer to the calorimeters.

- The overall magnetic shielding, chapter 6, is no longer a built-in part of the superstructure, but is one entity which is subsequently placed on the superstructure and bolted to it.
- The mirror alignment system, chapter 5, has been redesigned for ease of mounting of the mirrors and for greater stability with less material.

2 Optimisation of the optical layout

The final adjustment of the optical layout of RICH2 has been performed with the aid of simulation. This involves defining the position and radius of curvature of the spherical mirror, the position of the flat mirror, and the position of the photodetector plane. The detector is split into two halves, as far as the optical elements are concerned, on either side of the beam axis. Only one half of the detector is simulated, with reflection symmetry assumed about the plane $x = 0$. There is also reflection symmetry about the plane $y = 0$, with the elements tilted only in the xz projection: the centre of curvature of the spherical mirror, and the normals to both the flat mirror and the photodetector plane, therefore all lie in the plane $y = 0$. The coordinate system is given in figure 1.

2.1 Method

High momentum tracks are simulated originating from the interaction point and passing through the active acceptance of the detector (with polar angles $0 < \theta_x < 120$ mrad, $|\theta_y| < 100$ mrad in the xz and yz projections respectively). A uniform distribution of tracks is taken within these limits. Cherenkov photons are generated along the length of each track within the radiator volume, with Cherenkov angle fixed to the average value expected (31 mrad, given the refractive index of CF_4 gas in the wavelength region of interest for the photodetectors). The photons are randomly distributed in azimuthal angle. They are ray traced, reflecting off the spherical and flat mirrors of the detector, and their impact point on the photodetector plane is recorded.

The Cherenkov angle at emission is then reconstructed for each photon in turn, using the procedure developed for offline analysis: the photon detection point is used together with knowledge of the optics to calculate the Cherenkov angle by solving a quartic equation [2]. For this, the emission point is assumed to be at the midpoint through the radiator of the track that emitted the photon. As the true emission point was randomly distributed along the track, the reconstructed angle will not exactly agree with the true value. If the optical system was perfect, then all photons emitted from each track at a given azimuthal angle would be brought to the same point on the photodetector plane. The smearing of the reconstructed Cherenkov angle distribution thus provides a measure of the quality of the focusing. Its RMS is referred to as the emission-point error. This should be small compared to the other sources of finite resolution of the system, such as the pixellization of the photodetectors and the chromatic effect, from the dependence of the radiator refractive index with wavelength. The latter effect is the limiting factor for the resolution in RICH2, and corresponds to an uncertainty of 0.42 mrad on the Cherenkov angle per photon [2]. The optical elements of the RICH must therefore be set such that the emission-point error is small compared to this value.

In addition to the emission-point error, the optical layout determines the required area of photodetectors. For a given set of parameters, the area illuminated by the photons on the detector plane is inspected. The parameters are then adjusted to minimise this area, whilst maintaining an emission-point error that is acceptable. The constraints from the mechanical construction have to be respected, as discussed below. As there are seven parameters to adjust,

an iterative approach is applied, adjusting each parameter in turn until an optimal layout is found.

2.2 Constraints

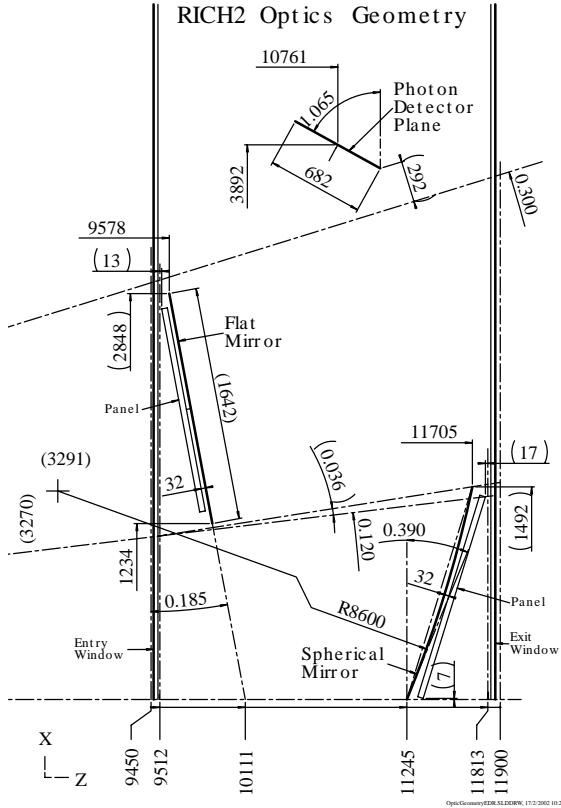


Figure 2: Half view of the optical geometry into the horizontal projection, the plane $y = 0$. Lengths are given in mm rounded to nearest millimetre. The angles are in radians. Numbers in () are calculated from the constrained geometry.

within the shielding structure. This was translated into a constraint on the position of the edge of the photodetector plane closest to the beam axis, that it should lie at least 288 mm outside the spectrometer acceptance limit.

The effect of varying the angle of the detector plane was studied during earlier iterations of the optical adjustment, and an angle of 1.065 rad (between the plane and the x axis, in the xz projection) was found to give a good compromise between the transverse size of the detector plane, the variation in emission point error across the plane, the requirements of magnetic shielding, and the preference that photons should strike the plane at close to normal incidence. This angle was fixed for the final iteration of the optics adjustment.

2.3 Results

The parameters that provided the best performance are listed here, and have been adopted for the definition of the engineering design of the RICH.

The spherical mirror has radius of curvature 8600 mm, with centre of curvature at (3270, 3291), where coordinates are given as (x, z) in mm. The transverse limits in the xz projection of the reflective surface that is struck by photons in the simulation are given by

The positions along z of the optical elements are constrained by the requirement that RICH2 fits within the space assigned to it within the LHCb spectrometer. The entrance and exit windows have finite thickness, and tolerances both from their construction and from the effect of the possible small pressure differences across them. Finally, space must be allowed for the thickness of the mirrors themselves, and their support structures. After accounting for these contributions which are given in chapter 5, the reflective surface of the spherical mirror must lie at $z \leq 11705$ mm, and the reflective surface of the flat mirror must lie at $z \geq 9578$ mm.

The tilt of the spherical mirror must be sufficient to ensure that the flat mirror lies outside the active acceptance of the RICH, i.e. $x > z \tan 0.12$. The photodetectors must lie outside the full acceptance of the spectrometer, i.e. $x > z \tan 0.3$, so that their material (and that of the substantial magnetic shielding that surrounds them) does not degrade the performance of the calorimeter system that lies behind RICH2. Furthermore, earlier studies of the magnetic shielding had demonstrated that sufficient performance of the shielding could only be achieved if the photodetector plane was further withdrawn

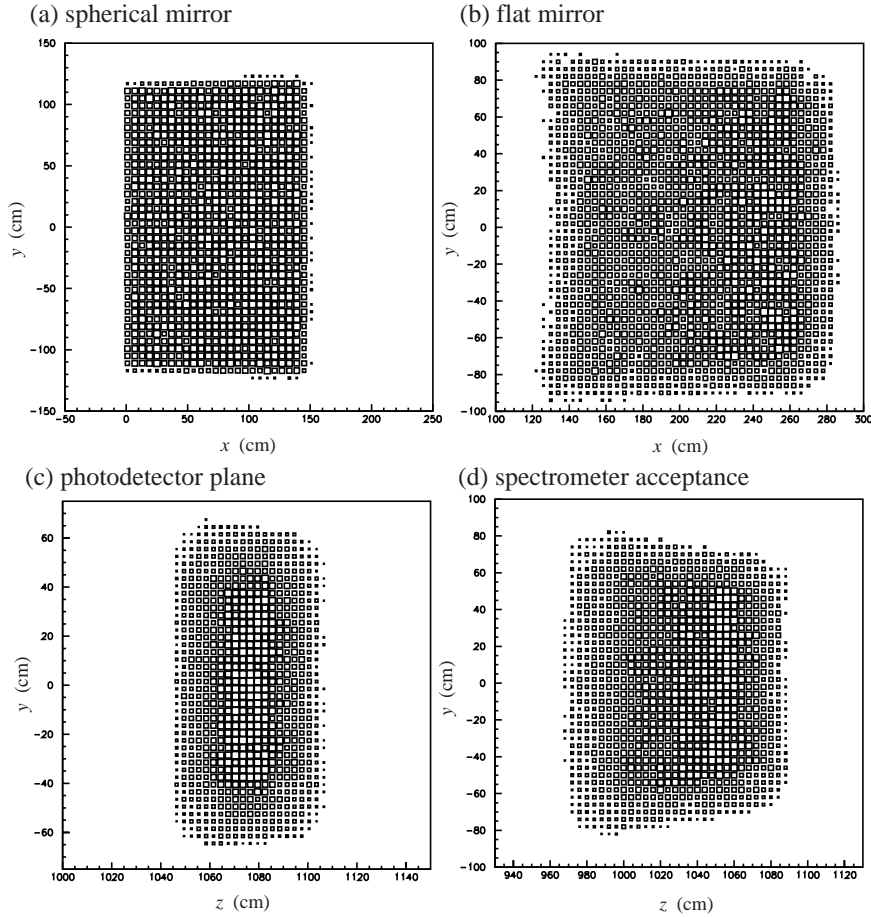


Figure 3: Hit density distributions of the impact point of simulated photons on various surfaces, where the area of each box is proportional to the number of photons landing in that region, and the axes are the standard coordinate system of the experiment: (a) the spherical mirror surface, (b) the flat mirror surface, (c) the photodetector plane (corresponding to the entrance windows of the HPDs), and (d) the plane defined by the spectrometer acceptance ($z = x \tan 0.3$) and the y axis; this is of interest for the layout of the photon funnel, figures 27 and 28, that supports the quartz window in front of the photon detectors.

(0, 11245) and (1492, 11705). For the flat mirror, the tilt of the mirror surface is 185 mrad with respect to the x axis, and the illuminated area has transverse limits at (1234, 9880) and (2848, 9578). The illuminated area on the detector plane has transverse limits at (3726, 11059) and (4057, 10462). This corresponds to a width of the plane in the xz projection of 682 mm, well matched to an array of nine columns of HPDs.

To determine the required extent of each element in the other dimension, the distributions of photon impact points are plotted in figure 3. To fully cover their distributions, the spherical mirror needs to extend to ± 1250 mm, the flat mirror to ± 950 mm, and the detector plane to ± 650 mm, along y .

With these parameters, the emission-point error is 0.25 mrad, comfortably lower than the limiting chromatic error. The number of detected Cherenkov photons per saturated track can be calculated assuming the photon detection efficiency discussed in the RICH TDR [2]. For an average reflectivity of 90% at each mirror, the number of detected photons varies across the acceptance between 21 and 27 per track. This is about 20% higher than the number quoted in the RICH TDR, due to an increase in radiator length that has been made possible with the

rearrangement of the LHCb tracking system since that time.

3 Super structure

The RICH 2 superstructure provides the support and location for the following components:

1. Spherical and flat mirror planes
2. Optics alignment system
3. Two photodetector assemblies
4. Magnetic shielding for photodetectors
5. Radiator gas enclosure, including gas inlet and outlet connections
6. Entrance and exit windows which themselves support a central tube surrounding the beam pipe
7. Two quartz windows providing the interface between the radiator gas and the photodetector assembly
8. The downstream end of the beam vacuum pipe.

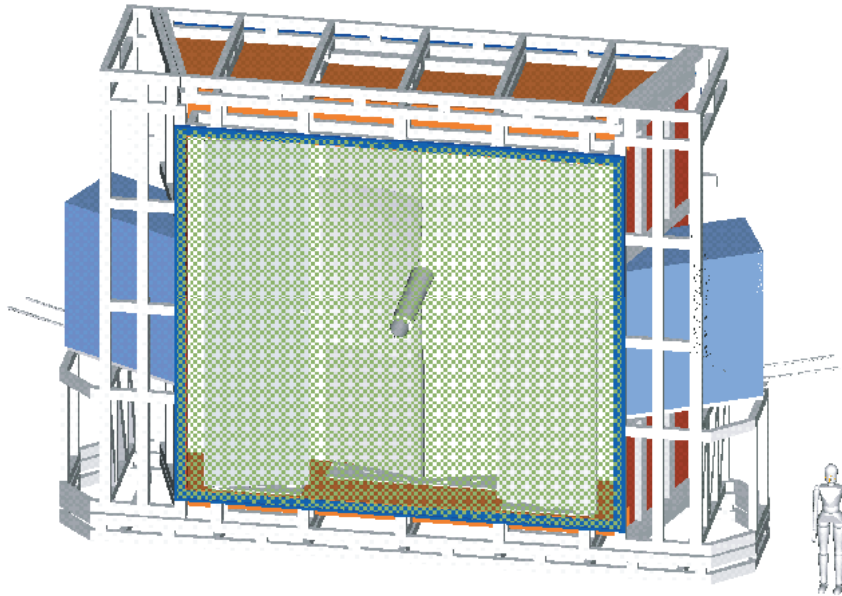


Figure 4: Full 3D CAD model of RICH 2.

Figure 4 shows a 3-D CAD model of the entire RICH 2 instrument, and figure 5 shows the superstructure separately. It comprises an open rectangular space frame lying entirely outside the acceptance of the LHCb spectrometer of ± 300 mrad in the horizontal plane and ± 250 mrad in the vertical plane.

A General Assembly drawing of the superstructure is enclosed in figures 23 and 24. The dimensions are derived from the optics layout drawings in figures 25 and 26, and from the space envelopes drawings in figures 27 and 28.

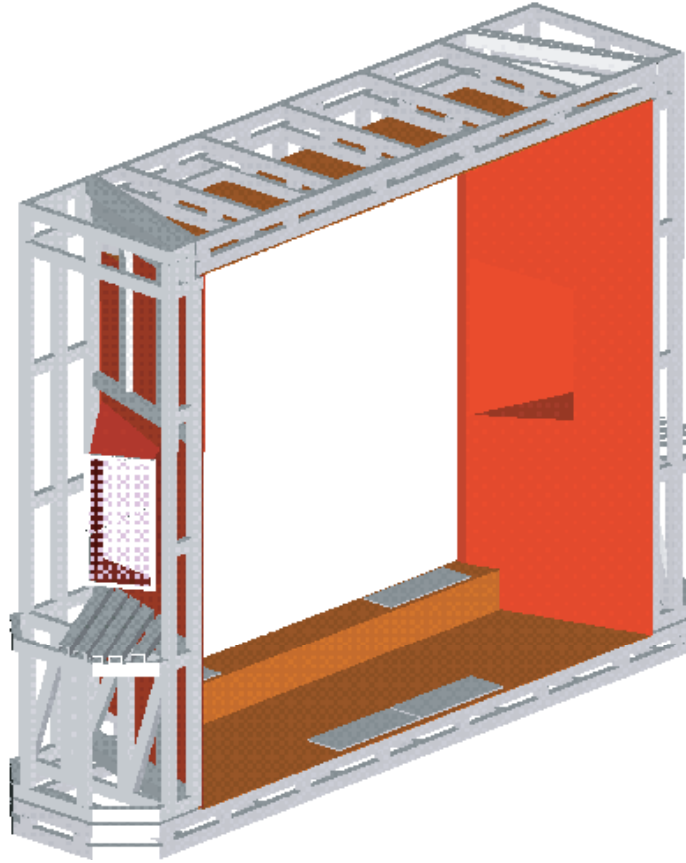


Figure 5: RICH2 superstructure and gas containment.

The superstructure is a welded construction of aluminium alloy rectangular hollow box section and the total weight of the structure is around 6000 kg. The top, bottom and sides are four separate fully welded constructions that will be transported to CERN and assembled on site. They will be bolted and doweled together, and the aluminium alloy sheet lining which provides the gas containment will be sealed together.

In order to minimise the manufacturing tolerances required for the structure, the window support frames will be aligned after assembly to achieve the required z -envelope. The frames will then be sealed and bonded into place as indicated in figure 31.

The magnetic shielding surrounding the photodetector assemblies will be bolted down to the superstructure. Deflections resulting from the magnetic forces on the shielding are shown in figure 6. A displacement of the top of the structure of 0.1 mm is calculated for the anticipated magnetic load of 5 kN on each of the shielding assemblies.

The structure is fastened to the floor of the experimental hall via the pedestrian tunnel structure as shown in figure 1. The four floor mounts are shimmed and surveyed into position, in order to achieve the required x , y and z locations with respect to the beam pipe and interaction point.

4 Gas windows

Two 5 mm thick quartz windows separate the radiator gas volume from the photodetector assemblies. Each window is made from two separate pieces of quartz bonded together via a

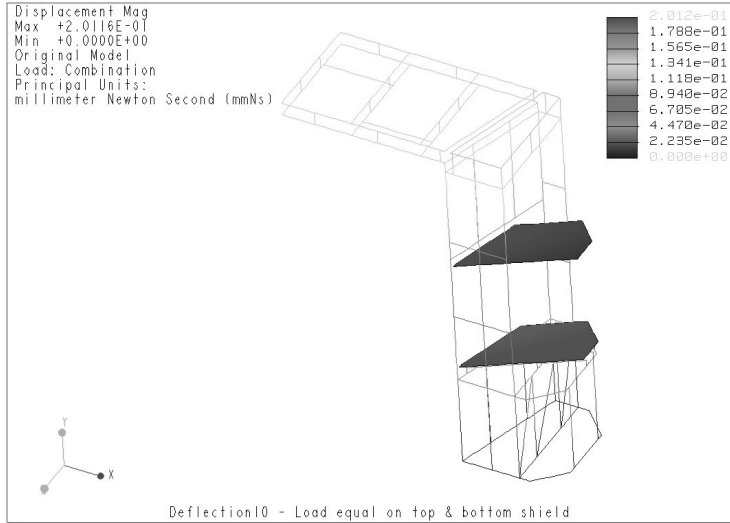


Figure 6: Deflections (mm) of partial structure under magnetic load.

narrow stainless steel 'I' section strip, and sealed into a frame as shown in figure 29. The joint between the two pieces is oriented along a line at 30° to minimise the reduction in active area for incident rays normal to the detector assembly, as shown in figure 30. The windows are fastened and sealed to flanges incorporated into two photon funnels, figures 27 and 28, which protrude from the gas containment box into the magnetic shielding as indicated in figure 23. The quartz will get a multi-layer dielectrics anti-reflection coating. A single layer of MgF_2 on a fused silica substrate reduces surface reflectance to less than 1.5% per surface over a broad spectral band. An example is shown in figure 9a.

The entrance window is a low mass composite panel made from two 1 mm thick carbon fibre reinforced epoxy skins separated by 28 mm thick polymethacrylimide (PMI) foam. Each skin is made from two layers of balanced weave laminate, with fibres oriented to give $0^\circ/90^\circ$ in one layer overlapped with $\pm 45^\circ$ in the other layer. This is in order to generate skins with as close to uniform a stiffness in the plane as possible. The radiation length for the entrance window is 1.0% X_0 .

The exit window is made from two 1 mm aluminium skins separated by 30 mm thick polymethacrylimide foam, giving a radiation length of 2.5% X_0 . The core thickness of the two panels is optimised in order to minimise the total z-space required for the windows, comprising the panel thickness plus the deflection resulting from the relative Cherenkov gas pressure of ${}^{+200}_{-100}$ Pa defined at the top of the detector.

The two windows are connected to each other by a central tube coaxial to the vacuum chamber. The tube is made from 2 mm thick carbon fibre epoxy composite, and has an inside diameter of 280 mm at the entrance window tapering to 330 mm at the exit window. This achieves a radial separation between the vacuum chamber and central tube of 45 mm, which is required to accommodate the heating jacket and thermal insulation which is needed during the bake-out of the vacuum chamber. Figure 7a shows a Finite Element (FE) analysis plot of the deflections of the windows and centre tube assembly resulting from an internal relative gas pressure of +400 Pa, i.e. using a safety factor of two at the top of the detector. The skins are assumed to have uniform properties in the plane. The entrance window is calculated to deflect a maximum of 10.3 mm in the entrance direction and the exit window a maximum of 23.3 mm

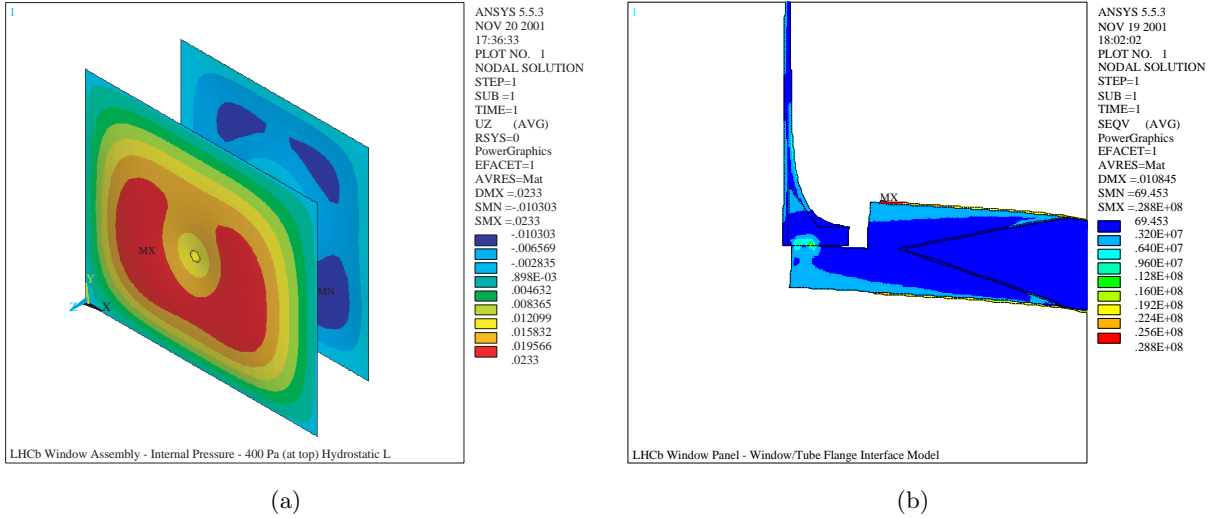


Figure 7: Deflection of windows and stresses on the centre tube joint due to a gas pressure relative to the atmosphere. (a) Deflections (mm) of entrance and exit windows due to radiator gas pressure. (b) Stresses (Pa) in entrance window to centre tube joint.

in the downstream direction. The flanged joint between the windows and centre tube is shown in figure 31. The joint is tapered in order to transfer the bending moment from the window skins into the thin centre tube. Figure 7b shows a plot from an axisymmetric FE model of the stresses in the joint components resulting from an internal relative gas pressure of +400 Pa.

Figure 27 shows the internal and external space envelopes required for the entry and exit windows, namely the window thickness, the internal and external deflections and the manufacturing tolerances. The deflections are assumed to be 25% greater than those calculated, due to the real properties of the composite panels observed in prototype tests compared with calculations.

4.1 Window Panel Manufacture and Prototype Testing

The windows will be manufactured from pre-cured laminate sheets, bonded together using a room temperature curing resin system and a partial vacuum. This method has been used to manufacture a 3 m × 3 m square test panel to the RICH TDR baseline specification, i.e. using two overlapping 0.5 mm thick glass fibre laminate sheets to make each skin with a 48 mm thick PMI core. This was pressure tested to 5500 Pa with the outer perimeter simply supported, at which point the deflection at the centre was 67 mm and small delamination blisters were observed on the surface under compression. This corresponds to a safety factor of around 5 in terms of stresses in the skins compared with the full-size window panels.

5 Optical elements

The design of the RICH2 is horizontally symmetric. On each side of the detector there is a spherical mirror surface of 4.1 m² and a flat mirror surface of 3.1 m² centred on the plane $y = 0$ as shown in figure 2.

The spherical mirror focuses the Cherenkov light in a horizontal acceptance of 0.12 rad and in a vertical acceptance of 0.1 rad. The flat mirror is used to reflect the ring image onto the photodetectors. The photon detectors are outside the horizontal acceptance of the LHCb

spectrometer of 0.3 rad. The reflective surfaces are made up of matrices of mirror segments. Each segment is fixed on an independent high precision adjustment support. It is in turn fastened on a large vertical panel as shown in figure 8.

5.1 Optical geometry constraints

Apart from the main constraint which are imposed by the physics performance as described in chapter 2, position of supports and other mechanical elements will give further limitations for the optimisation of the optical geometry. Since the design and the mechanical characteristics have now been established in detail, the clearances have been fixed for the positions of the mirrors and the photon detector planes.

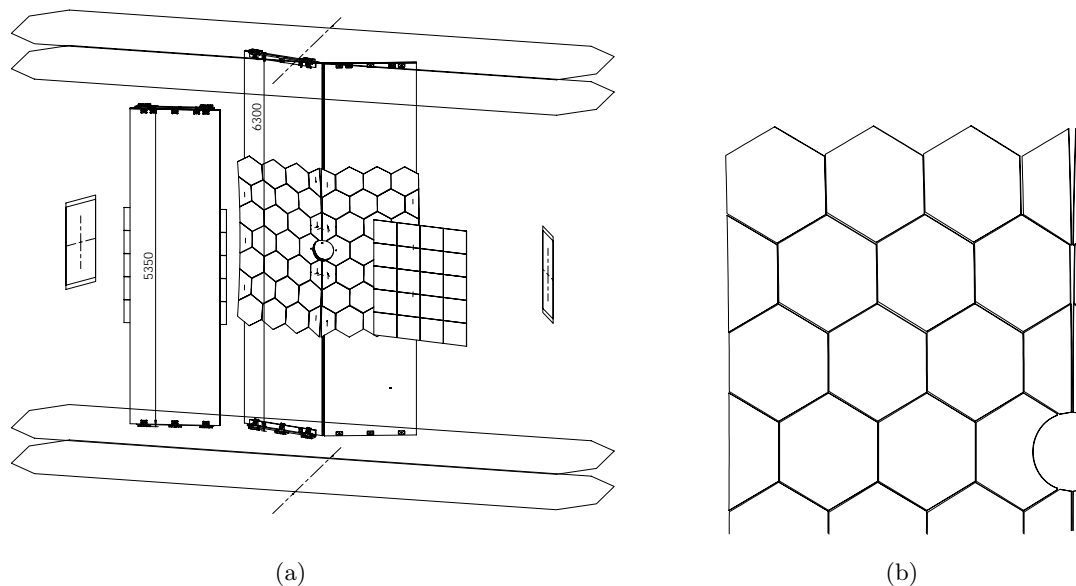


Figure 8: (a) 3D view of the mirror arrays and their support panels. The bearing length for panel fastening: spherical mirrors: 6300 mm - flat mirrors: 5350 mm. (b) The close packing of the spherical mirrors.

The closest edge of the spherical mirrors to the exit window has been fixed at $z = 11705$ mm in order to get enough room to position a flat panel and supports to hold the spherical mirror segments. This flat panel is tangential to the middle of the spherical mirror surface. A distance of 32 mm from the reflective surface is needed for the mirror supports. The mirror segments which are located at the edges of the acceptance, require a panel width of minimum 1480 mm. The edge of this panel is at 17 mm from the envelope of the exit window. This clearance allows the adjustment of the whole spherical mirror array to compensate for any manufacturing, assembling and positioning errors. The exit window envelope includes: an internal clearance of 4.5 mm, the deflection due to the relative gas pressure and manufacturing and positioning errors. The opposite edge of the support panel comes close to the symmetric zy -plane. Due to the symmetric design of the RICH2, an identical panel is placed on the opposite area. The clearance between these neighbouring panel edges is 14 mm.

For the flat mirror surfaces, the closest edge to the entry window has been set to $z = 9578$ mm. A panel, holding the mirror segments is parallel to them and located at 32 mm from the reflective surface. This distance is required by the mirror supports. This design gives a clearance of

13 mm to the entry window limit to allow for adjustment. The entry window envelope includes an internal clearance of 4.5 mm and others tolerances as described in chapter 3.

The operation of the photon detectors, the HPD matrix, will require a magnetic field below 10 gauss. Magnetic field simulations have shown that the magnetic field can be reduced to this value in a volume located inside a magnetic shielding box. See chapter 6. This low field region can be obtained at a minimum distance of about 28 cm from the 0.3 rad acceptance of the LHCb spectrometer with a shielding box surrounding this region and extended to the acceptance limit. The photon detector plane is tilted by 1.065 rad with respect to the x -axis. This is a compromise between the optical, mechanical and the magnetic shielding requirements.

5.2 Spherical mirrors

Each of the spherical mirror matrices is composed of 21 hexagonal mirrors and 7 half hexagonal mirrors. The size of the mirror segments, with spherical radius of curvature of $8600 \text{ mm} \pm 0.5 \%$, has been adapted to fill the required acceptance of $x = 0$ to 1492 mm or from 0 to $120+36$ mrad. The mirrors are rotated in order to be as close as possible to the vertical symmetry plane $x = 0$ as shown in figure 8b. The flat to flat of the hexagonal mirrors is 441.67 mm for a circumscribed circle of diameter $\varnothing = 510$ mm. The half segments are exactly half of the same hexagon from corner to corner. The mirror segments have been mapped with minimum clearances of 4 mm between side-by-side mirrors. The closest segments to the symmetric yz -plane are also at a minimum of 4 mm from a neighbouring segment. These gaps are necessary to avoid any conflict between two adjacent mirrors due to the machining and assembly errors of panels, supports and mirrors. The mirror rotation implies a translation. See chapter 5.7. It is taken into account in these clearances. This segment mapping gives a total reflective surface of 96.2% compared to the photon impact analysis of $x = 0$ to 1492 mm and $y = \pm 1250$ mm. The effective reflective surface includes 1% loss due to tolerances of the segment sizes and chamfers. The two hexagonal mirrors and the four half-hexagonal mirrors near the central tube, chapter 4, will have a circular cut-out in order to surround this tube with a clearance of 7 mm from an estimated diameter $\varnothing = 326$ mm. This last surface loss represents 1.3% of the reflective surface.

5.3 Flat mirrors

To cover one flat mirror surface, 20 rectangular mirror segments of $410 \times 380 \text{ mm}^2$ will be used with clearances of 4 mm between side-to-side mirror segments, figure 8a. The segments will extend respectively 5 mm horizontally and 8 mm vertically, the minimum reflective surface in order to compensate any errors of mirror segment positioning. The reflective surface efficiency is 97.5% of the required coverage $[x, z]$ [1234, 9880] to [2848, 9578] for $y = \pm 950$ mm. This efficiency includes the tolerances of the segment size and chamfers.

5.4 Mirror specifications

The spherical and flat mirrors have a thickness of 6 mm made of a glass substrate like Simax¹ or Pyrex². See also reference [13]. The size tolerance is ± 0.25 mm with a chamfered edge of < 1 mm. The reflective surface should have a roughness better than 3 nm. This face will be coated with aluminium and a MgF_2 or SiO_2 protective layer. The surface efficiency indicated above does not take in account the efficiency of mirror coating quality itself. The reflectivity is assumed to be approximately 87% between 250 to 500 nm and better than 70% at 210 to 250 nm over a broad range of incident angles centered around 0.4 rad to the spherical mirror and around 0.8 rad to the flat mirrors as shown in figure 9b.

¹3.3 borosilicate glass by SKLÁRNY KAVALIER, a.s.

²Borosilicate glass composition by Corning Incorporated.

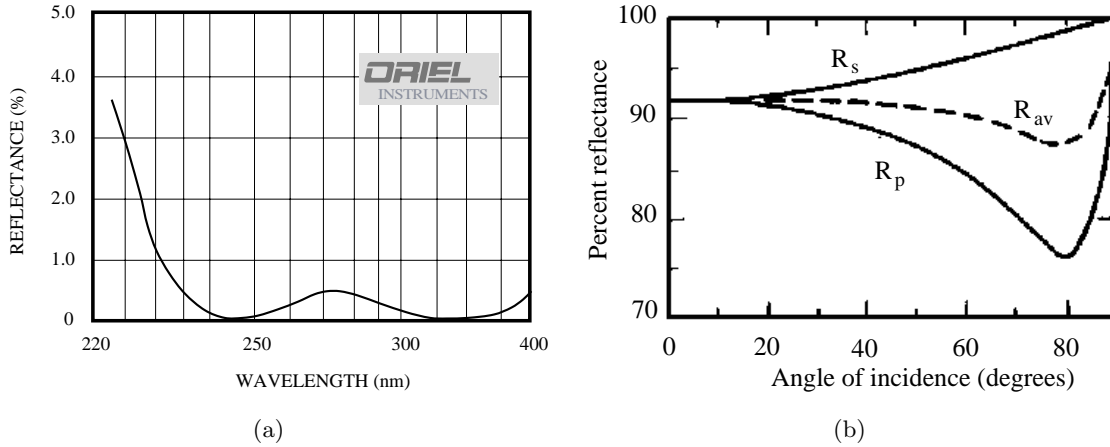


Figure 9: (a) Typical reflectance of 79700 coating on a fused silica substrate. Because of the high number of layers, these coatings are more sensitive to incident angle than the single layer MgF_2 coatings. <http://www.oriel.com/netcat/VolumeIII/pdfs/v36ar.pdf> (b) Calculated reflectance of Al as function of incident angle at $\lambda = 546 \text{ nm}$ [5]. The subscripts s and p refers to light polarised perpendicular and parallel, respectively, to the plane of incident. $R_{av} = \frac{1}{2} [R_s + R_p]$.

5.5 Sandwich panel

Large aluminium sandwich panels, figure 10a, support the spherical and flat mirror matrices. They ensure good positioning and high stability of all mirror segments for a long radiation length. See table 2 given at the end of this note. These panels are flat and fixed at the bottom and at the top to the superstructure inside the vessel. The panels are made from 38 mm thick aluminium honeycomb core which is embedded between two aluminium sheets, skins, of 1 mm thickness. The hexagonal cell size of the core is 6.4 mm for a density of 83 kg/m^3 . There are slots on both sides of the core to avoid any pressure difference and enclosed air volumes that might pollute the fluorocarbon gas. Rectangular aluminium bars are embedded between the two skins at the bottom and top ends of the panels. These reinforcement bars allow machining operations, after bonding, for fixation points at the extremities of the panels. After these operations, the mirror support fixation points will be machined into the panels. The rectangular aluminium bars are at the minimum 15 mm outside the 0.25 rad acceptance limit of the LHCb spectrometer. With these considerations, the panels, figure 10, have the following dimensions: the panel for the spherical mirrors: 6200 mm height by 1480 mm width and for the flat mirrors: 5250 mm height by 1480 mm width. The height of the panels for the flat mirrors are slightly reduced compared to the RICH TDR [2]. This has been done in order to increase the stiffness of the panel while staying outside the acceptance with the supporting structure.

A finite element analysis of a populated panel including the mirror weight, gives a deflection smaller than 0.2 mm. The first three natural frequencies are respectively 2, 10, and 12 Hz. See figure 10b.

Due to the panel size and the fact that we only need four pieces, an industrial manufacturing process can not be readily envisaged. We have therefore executed a number of smaller test panels. A peel test has shown that with an epoxy Araldite 420AB (400 g/m^2) polymerised at room temperature and with abraded skin surfaces, the resistance of the sandwich was limited by the tearing of the aluminium core. Since the panels are inside a dry atmosphere, no particular surface treatment of the aluminium is required to prevent corrosion that could damage the bond adhesion. To check the flatness that can be obtained, we have produced a $0.5 \times 2.5 \text{ m}^2$ sample.

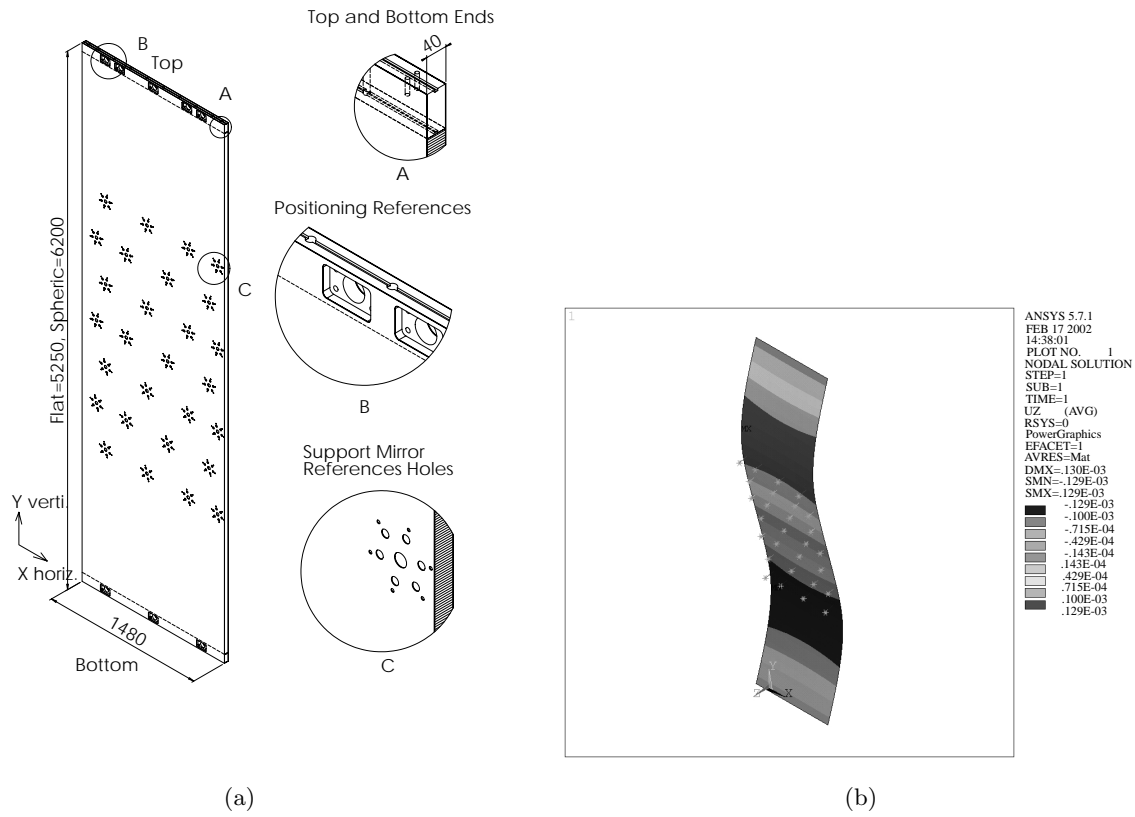


Figure 10: The aluminium honeycomb mirror panel. (a) Honeycomb sandwich panel for holding the mirrors. (b) Static deflection of panel due to mirror weight.

The surface flatness was 0.3 mm. We can therefore expect a flatness of ~ 1 mm for the final panels. It was initially foreseen to embed inserts inside the panels to stiffen the area where the mirrors are fixed. Stability measurements on panels of 0.5×0.5 m² have been performed. No real relaxation difference between including or not including the insert, can be observed over a time period of 10 days. As the inserts are not required, it simplifies the manufacturing process of these sandwich parts. Our bonding tests have demonstrated the difficulties for manufacturing large sandwich panels without adequate facilities. The main difficulties are the short pot life of the epoxies, the procurement and the handling of large thin sheets in addition to the need for a perfectly flat working surface. Contacts with industry have taken place in order to investigate the manufacturing possibilities of these panels.

5.6 Panel positioning mechanism

An adjustment system, figure 11, of the sandwich panels supporting the mirror segments is needed to approximately align them. As the panels are fixed at the bottom and at the top of the structure, this mechanism must compensate for all misalignments along the x, y and z directions. Errors could arise from the positioning of the sandwich panels themselves, the mirror supports, the machining references on the structure and the position of the structure with respect to the LHCb co-ordinates. The adjustment range is ± 8 mm in all directions from a nominal position and the panels can be positioned to approximately 0.5 mm or to within 0.5 mrad. In order to be less dependent on the structure, the panels are seated on the superstructure and

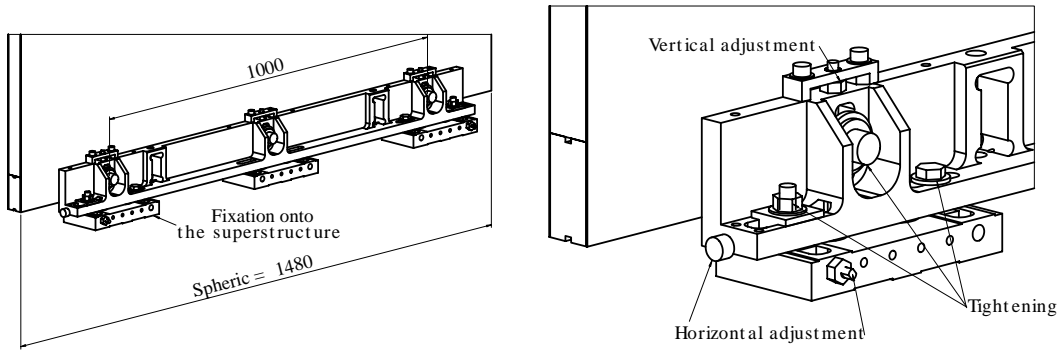


Figure 11: Mechanism for panels positioning.

not suspended by it. The vertical reference is given by the bottom mechanism. The top is free for a limited vertical movement, ± 2.5 mm, to absorb any possible thermal expansion difference between the panels and the structure. At the top, a vertical pull of $\sim 2 \times 500$ N is given by spring washers in order to compensate any friction in the mechanism. The vertical extension of the mechanism is as compact as possible, in order to limit the height of the structure. As the panels come very close to the external window envelope, the adjustment parts are accessible only from the mirror side. After adjustment, the mechanisms are fully tightened on the structure and the panels are also fully tightened at the bottom on the panel positioning mechanisms. No stress is expected because all parts are made of aluminium and we do not expect any local temperature gradient.

5.7 Mirror support

The mirror supports are the crucial elements that will allow the construction of a near perfect reflective surface from the mirror segments. The initial alignments of the mirrors must be better than 1 mrad to have a negligible effect on the Cherenkov ring reconstruction as discussed in chapter 9. These supports are the interface parts between all mirror segments and the flat sandwich panels. In contrast to the flat reflective surface where all supports are identical, the spherical reflective surface requires customised supports for each mirror segment.

A new mirror support has been developed and tested since the RICH TDR [2]. This new mirror support is shown in figures 12a and 12b. It has been proposed in order to get a larger adjustment range to compensate for any misalignment and for easier positioning of the mirrors. The support is based on a system of three attachment points (F). Each attachment point is adjustable and gives a rotation around the axis defined by the two other points.

The main parts (E, G, H) are made of polycarbonate for its low fraction of a radiation length, robustness, stability and compatibility with the fluorocarbon gas. The support is fixed to the panel with aluminium screws and nuts (A, B, D). Screws, nuts and spring washers (F) compose the adjustment mechanism. These parts are made of steel, brass and aluminium. To allow the dismounting and interchangeability of the mirrors, the flange (H) is bonded on the mirror (I) and fixed by screws (L) on part (G). In this design, each adjustable point is not a spherical joint. The system might therefore theoretically be overconstrained. This constraint can be admitted as the translation is very small and the clearances between the parts can absorb it. To minimise the backlash of the mechanism (F), there are spring washers at (M). To have a small translation of the attachment point we use a differential screw system. Figure 13 shows the principle. (A) is a screw with two different pitches corresponding to α and β angles. (B) and (C) are the nuts. In our design, one pitch is $\tan \alpha \cdot d\gamma = 0.75$ mm and the other pitch is $\tan \beta \cdot d\gamma = 0.70$ mm,

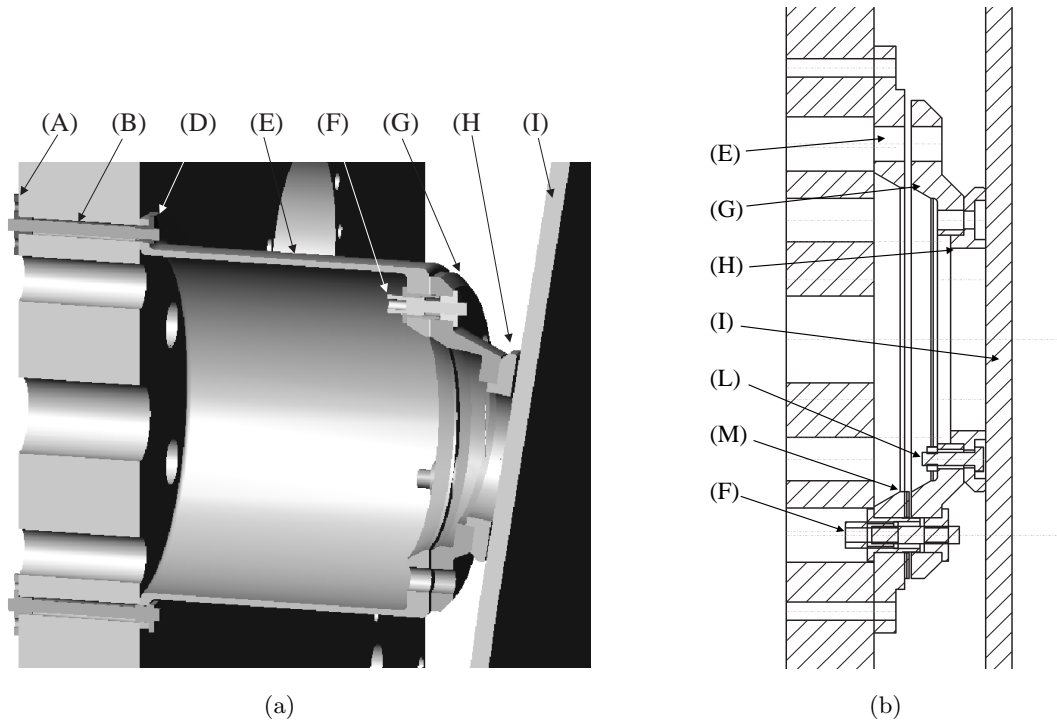


Figure 12: Mirror adjustment mechanism. (a) View of the support for a spherical mirror segment. (b) Cross section view of the support for a flat mirror segment. See text for the definition of the different elements.

then $dx = 0.05 \text{ mm}$ for $\Delta\gamma = 2\pi$.

The measurement of adjustment characteristics on a support for a flat mirror is shown in figure 14a. The action gives a smooth motion, quite rigid, easy to adjust and without hysteresis. The adjustment resolution, $d\delta$ is 0.7 mrad with a $\text{RMS} = 40 \mu\text{rad}$ for each screw turn as shown in figure 14a. The crosstalk between a horizontal and a vertical movement has a $\text{RMS} = 6 \mu\text{rad}$ with a maximum excursion of $\pm 20 \mu\text{rad}$ over the full adjustment range of $\pm 5.5 \text{ mrad}$.

A two month long stability test has been done on the mirror support. The result is shown in figure 14b. It is adequately stable. Other measurements [7] and [8] have demonstrated that the main relaxation occurs during the first five days. After 60 days we have a vertical angular deviation of less than $40 \mu\text{rad}$. This deviation is affected mainly by the temperature change of 2°C . During a stable temperature period with $\Delta T < 0.5^\circ\text{C}$, the movement of the support was less than $10 \mu\text{rad}$. It is therefore reasonable to assume that the frame which was supporting the sample could be responsible for this displacement. It has also been noted that there is a correlation between the humidity and the global stability of the optical bench.

The mirror support parts are mainly polycarbonate placed in the CF_4 gas. The compatibility of this type of polymer with a fluorocarbon gas has been verified. Samples of polycarbonate were immersed in C_6F_{14} vapour at $\sim 40^\circ\text{C}$ during 7 and, for some of the samples, 21 months. No measurable change in mechanical characteristics, such as weight, dimensions, tensile strength and elasticity modulus, could be observed.

5.8 Assembly

All assemblies and adjustments of the optical elements can only be made when the windows are removed. Adequate room must be available to put scaffolding inside and outside the vessel for

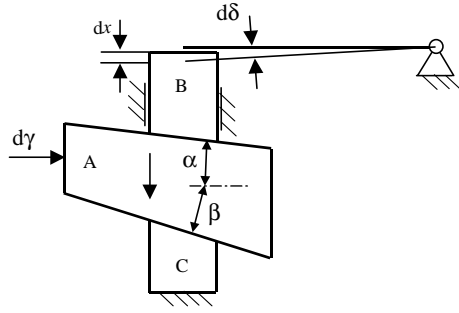
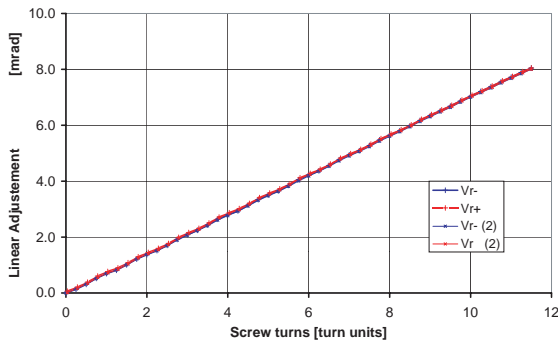
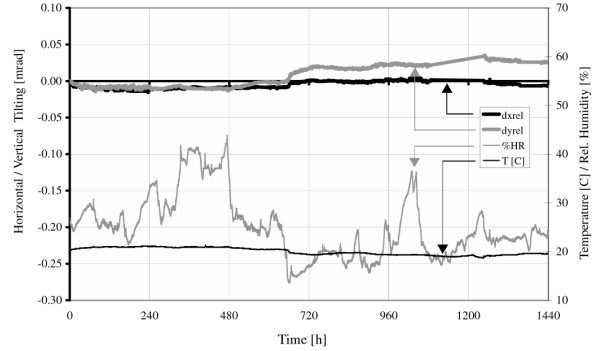


Figure 13: Principle of differential translation used for the mirror support.



(a)



(b)

Figure 14: Stability of mirror support. (a) Adjustment of the mirror support. $-$ is the trigonometric direction, $+$ is the clock direction. The measurement is repeated twice. (b) Stability measurement of mirror support during 60 days. dx_{rel} and dy_{rel} are relative displacement of the sample compare to the reference respectively in respectively the horizontal and the vertical direction.

the mounting of the optics elements. Details of the mounting sequence and the survey procedure are given in chapter 8.

Since all clearances are kept minimal, particular care will be required when the windows are to be installed and when the central tube is fixed to these windows.

6 The magnetic shield

The RICH2 detector is almost halfway between the 1600-ton iron yoke of the dipole and the massive ferromagnetic structure of the hadron calorimeter as shown in figure 1. The maximum stray field in the region where the HPDs will be located, is therefore of more than 150 gauss and is rapidly varying in all directions.

An HPD tube without Mumetal³ shield is magnetic field tolerant up to about 10 gauss. A single tube with Mumetal shield can tolerate a magnet field in the order of 30 gauss. A matrix of HPD tubes with their shields included, can give rise to saturation effects. Our aim is therefore to reach a magnetic field that do not exceed 10 gauss surrounding the HPD matrix by using an external shielding box. We have designed an iron box, able to attenuate the field of the dipole by a factor of ≥ 15 .

³Mumetal - Magnetic Shielding Alloy (Ni77/Fe14/Cu 5/Mo 4)

An accurate simulation must keep into account the general behaviour of the field and the complete assembly of the experiment, although the actual magnetic field in the experimental area will depend on several parameters that can not be included in the simulation model. A TOSCA [9] finite element model of the full LHCb layout has been prepared and run with our shield integrated in it. However, to get a first approximation with quicker finite element calculations, we began with an ANSYS [10] simulation in a constant vertical field of 150 gauss and, only after this step, this first approximation shield was included in the full TOSCA simulation.

From that point on, several iterations were necessary to get the required performances. The iterations were able to define a suitable shape and disposition of the shield at a precise angle with respect to the mirror orientation, keeping into account the constraints of the mechanical assembly, of the cable routing, of the super-structure. The influence of the material properties on the general shielding performances was also studied. The outline of the optimised shield is shown in figure 15a, its mass will stay below 6 tons per side.

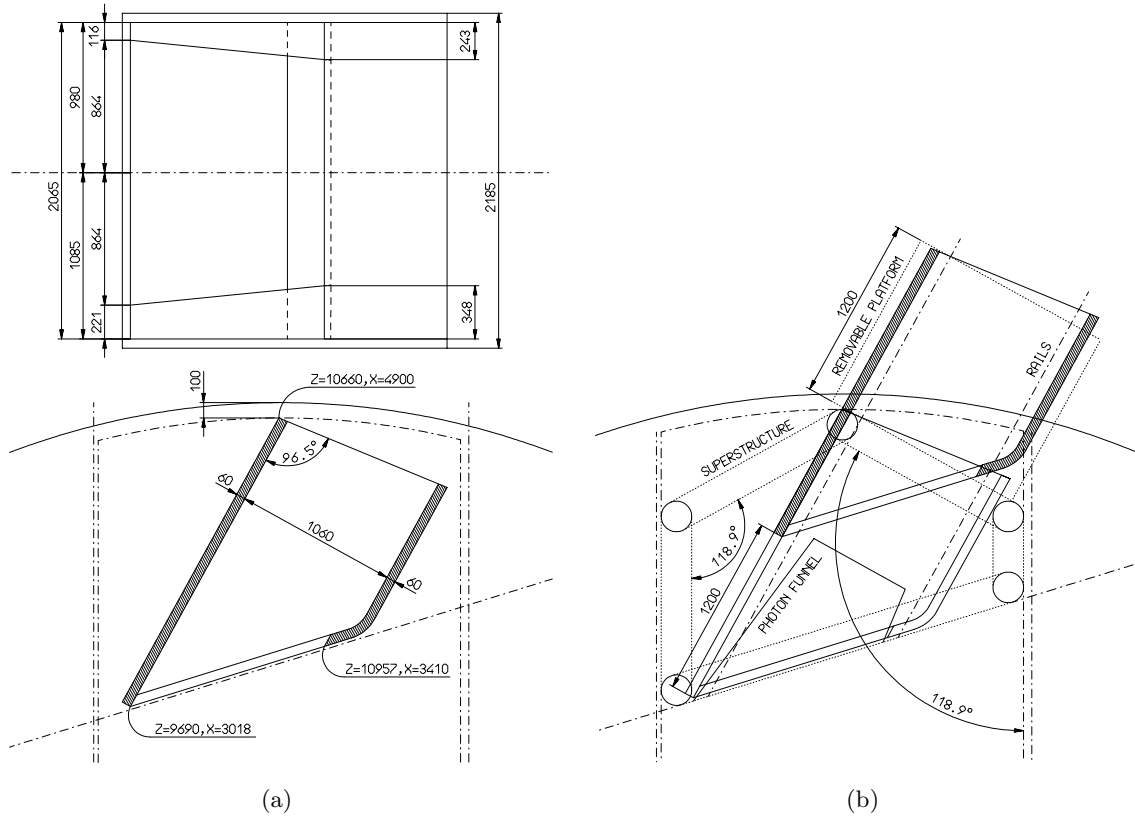


Figure 15: The overall magnetic shielding. (a) Outline of the optimised magnetic shield. (b) Installation scenario for the overall magnetic shielding.

Given that the photon funnel, figures 27 and 28, which is the support of the quartz window, will be installed before the magnetic shield, the latter has to be slid over the photon funnel. To do this, the shield is mounted on standard carriages, running on rails, as suggested in figure 15b. A first segment of the rails belongs to the superstructure, while a second segment belongs to a removable external platform, allowing a total stroke of 1.2 m. Once the shield is pushed in the working position, it will be lifted by means of jacks (much less than the clearance of 10 mm), the carriages will be replaced by aluminium blocs and the shield will be bolted to the superstructure.

We did not include into the simulation model the cylindrical Mumetal shields around the

HPDs. As the field level is below 10 gauss inside the main shielding structure, the presence of these local shields can only reduce the external magnetic field inside the HPDs. Another reason was that the geometric dimensions of the Mumetal sheets (about 1.0 mm thick) made it impossible to use the general complete model to calculate the field in the Mumetal. However, a sub-modelling analysis is under way, with the aim of generating field maps in a simulated region that is large enough to keep into account the 3D aspect of the field and including the Mumetal shields as well.

The maximum computed values of the magnetic field at different horizontal planes are reported in table 1, in the region identified as the good-field one. In order to give easy access for cable routing and assembly needs, also the influence of the removal of the rear plate is reported in table 1.

The shielding structure will be closed on the cavern side by a light tight door that will also be nearly gas tight. Light and gas sealing will also be done on the photon funnel side. Inert gas will be circulated in this enclosure. A patch panel for signal and power links will be placed on the high-z side of the shielding structure. This disturbance to the shielding has not yet been quantified, but it is not assumed that it will change the shielding efficiency measurably. The power dissipation inside each of the structures is ~ 500 W. See table 4 given at the end of this note. We believe that the inert gas circulation will remove this power. If it should prove indispensable, it is easy to provide a cooling shield on the top and bottom of the structure.

	$y = 0$ cm	$y = 40$ cm	$y = 74$ cm
With rear plate	4.1 G	6.4 G	7.2 G
Without rear plate	5.8 G	8.7 G	9.4 G

Table 1: Maximum magnetic field values inside the RICH 2 box. Model according to drawing MagneticShielding_010718A.

In figure 16 we have also reproduced an example of a computed field map.

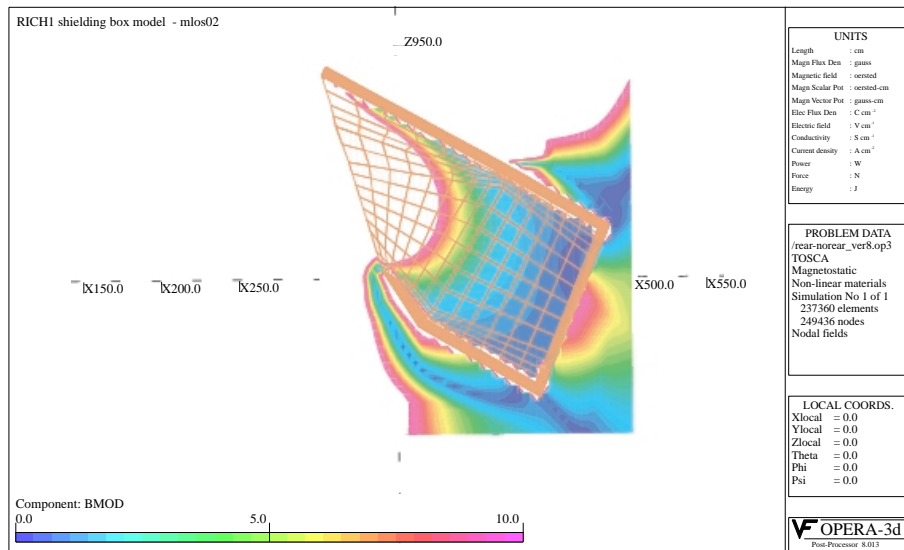


Figure 16: Example of a computed field map.

7 Photon detector plane

7.1 General description of the system

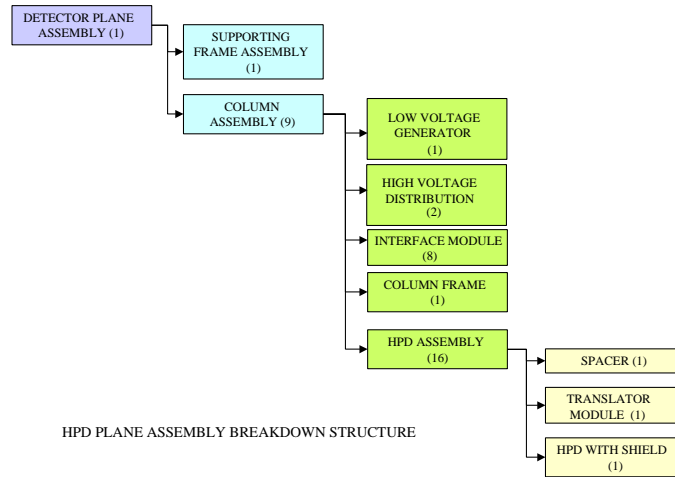


Figure 17: HPD plane assembly breakdown structure.

A detailed design of the HPD supporting structure has been developed after the outline in [2] and [11]. "Modularity" is the basic concept of the detector structure. Figure 17 outlines the detector plane assembly breakdown structure, while figure 18 shows the column assembly exploded view and figure 19 the detector plane exploded view.

Every HPD, with its own Mumetal shield, is centred and fastened on a spacer made of glass-filled Nylon, by means of screws and dowel pins. The spacer is centred and fastened on a column frame, made of aluminium profiles, by means of screws and dowel pins. The HPD subassembly is outlined in drawing LHDRW0003S as shown in figure 32. Every column carries also level 0 electronics (*Interface module*) and LV and HV distribution boards (*Low Voltage generator* and *High Voltage distribution*). A column can carry up to 16 HPDs, but 15 could be enough to cover the required sensitive area.

The HPD electric pins fit into a Zero Insertion Force (ZIF) socket. It is a standard Socket 7⁴, which is operated without the lever. The ZIF socket is fitted on the *Translator module*, a multi-layer printed circuit board that carries on its other side a linear 64 pin dual rows connector. The routing for the socket and for the connector have to be compatible. A twisted pair flat cable with connectors at both ends link the *Translator module* to the *Interface module*, through a groove foreseen on the column frame. The spacer features openings to allow the heat to be drained away from the *Translator module* by natural convection. Every HPD has its own independent *Translator module*. HPD HV cables come out from the HPD rear plate and are routed to the *High Voltage distribution* on the side of the column frame.

Up to 9 columns can be fitted in the supporting frame assembly, where the nominal HPD pitch is 87 mm. The requirements associated with this pitch are such that the HPD assembly will meet the required tolerances, section 7.2. The HPD array will be made up of $9 \times 16 = 144$ or $9 \times 15 = 135$ detectors. The column assemblies are centred and secured to the supporting frame assembly, made of aluminium profiles, by means of screws and dowel pins; the system is designed so that every column assembly can be pulled out independently from the back side of the panel, sliding on its guides. Once a column is out of the frame, it is relatively easy to disconnect and

⁴Socket 7 is the descriptive term for the way certain Intel Pentium microprocessors plug into a computer motherboard so that it makes contact with the motherboard's built-in wires or data bus.

slide out every *Interface module* independently. The column subassembly is outlined in drawing LHDRW0002S as shown in figure 33.

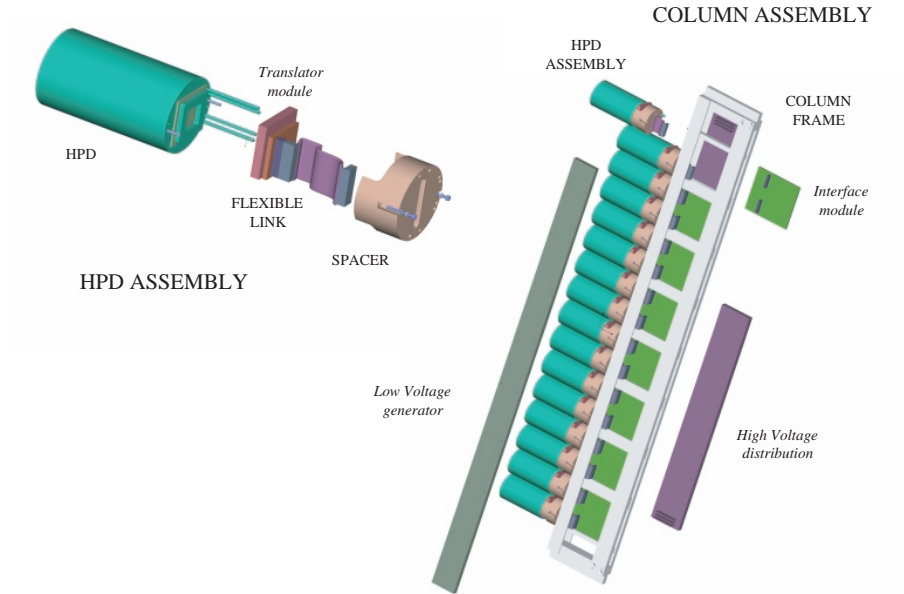


Figure 18: Column assembly.

The supporting frame assembly features three concentric frames, so that the detector plane position can be adjusted (on its plane) by means of a system of sliding wedges and adjusting screws; the available run is ± 2 mm. The adjusting knobs are located on the top and on the bottom side corner of the external frame.

The detector assembly stands on a trolley sliding on rails fastened to the overall magnetic shield, and can be easily pushed into its operating position or pulled out to a convenient maintenance area. Only minor maintenance, such as the substitution of a card, is advisable in the pit. A set of levelling screws allows the detector assembly orientation to be adjusted. The detector plane assembly is outlined in drawing LHDRW0001S as shown in figures 34, 35 and 36.

HV main cables, linked to the *High Voltage distribution* cards, are routed to the top and bottom of the detector assembly rear side, leaving enough free space to access the electronics. These cables link individually all *High Voltage distribution* modules to a patch panel with connectors, located on a side wall of the overall magnetic shield, that works as a junction box.

7.2 Interfaces

An "HPD mechanical interface requirements" note is being circulated, where shape envelopes, dimensional and shape tolerances, cable and hole positions are tentatively proposed [12]. That document refers to the HPD with its magnetic shield integrated as a whole. An optimisation process will now start to make sure that all needs around the photon detector plane are fully satisfied. Preliminary considerations about the complete assembly process have been made, in order not to state any unachievable requirements. This specification allows to set the HPD pitch to a nominal value of 87 mm and make due allowances so that the HPDs will fit into the supporting structure with reasonable clearances and to ensure a safe installation, operation and removal of the modular elements.

With the same philosophy, interface requirement drawings are being discussed to agree on the allowable shape and dimensions of every printed circuit board to be integrated into the

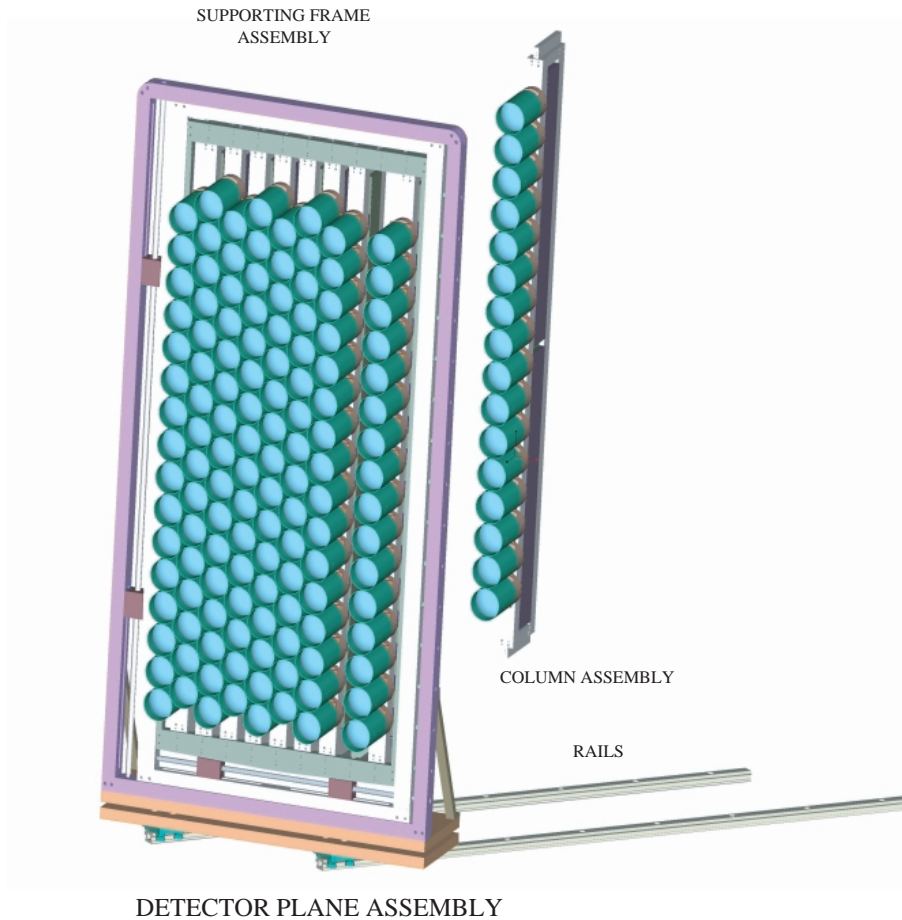


Figure 19: Detector plane assembly.

detector plane structure.

A modified version of ZIF Socket 7 is required. It is derived from the standard one but with no lever. Assumptions have been made about overall dimensions and interface requirement drawings are circulating.

The photon detector plane has been designed and optimised around the base line photon detector, the HPD. In the unlikely event that the HPD project should fail the milestones which will trigger a change of photon detectors, it is reasonably straight forward to accommodate a MAPMT matrix in the same structure.

8 Procedure for mirror wall survey and alignment

The spherical and plane mirror walls of RICH2 will have to be precisely aligned in order to obtain the required resolution on the Cherenkov rings and to fully exploit the photodetector capabilities [13]. Each spherical and flat mirror has to be aligned with respect to the other mirrors to form spherical and plane walls as shown in figure 20. They must have their centres of curvature⁵ pointing to the centre of the photodetector. The spherical and flat surfaces have therefore to be aligned one with respect to the other and both with respect to the particle beam axis. The optical alignment will be first carried out in a suitable laboratory and will be checked once, when the RICH2 is lowered and placed in the experimental area. It is not reasonable to

⁵For the flat mirrors, this is the axis normal to the plane.

perform a complete survey and alignment in the pit as the space required is large due to the radius of curvature of the mirrors and the difficulties in having a clean and dust free environment.

The optical alignment procedure can be summarised as following:

1. The super structure is surveyed and reference axes and focal points are defined, as well as the position of the mirror support walls.
2. Mirrors are mounted and the spherical walls are aligned with respect to the focal points, without the flat walls and by means of a laser point source.
3. Flat walls are mounted and the point source is moved into a point situated roughly on the particle beam axis. The flat and spherical walls are now aligned to generate a single image point on the axis normal to the photodetectors plane. This will allow also a measure of the total astigmatism of the system.

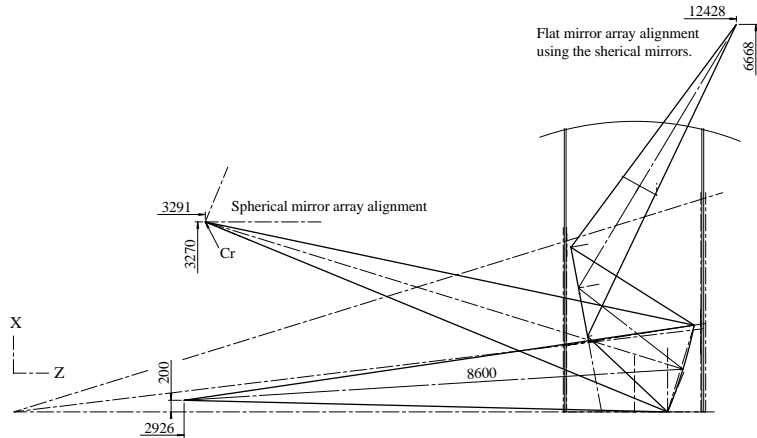


Figure 20: Schematic drawing of the survey and alignment system.

8.1 Survey and reference axis

On the super structure (with simulated photodetector housings) a few fiducial points are defined and their distance is measured with respect to each other. These points have to be stable and will be the references to the alignment of RICH 2 to the beam axis and the general coordinate system of LHCb as given in figure 1. The centres of curvature of the mirror walls can now be defined in this system, Cr_i (with $i=1, 2$ which refers to the two mirror walls in figure 8). At this point, the spherical mirror wall plates are mounted on the super structure. In their fixations to the super structure, they retain a limited rotation freedom (see chapter 5) around their vertical symmetry axis, allowing for an adjustment with respect to the Cr_i points as shown in figure 20. Any deformation of the super structure before and after the insertion of the mirror wall panels will be controlled and the reference system modified accordingly. The normal starting at Cr_i and ending at the centre of the mirror wall (which will coincide by construction with the centre of the mirror wall plates) is the centre of curvature axis \hat{u}_i . As Cr_i is at 8.6 m from the mirror wall plates, a laser beam, crossing Cr_i , will define \hat{u}_i and its back reflection from the mirror wall plates will provide a first adjustment. With a suitable laser translation system, a few points on the mirror wall plates can be probed and both mirror wall plates, therefore, adjusted with precision. If an uncertainty of < 1 mm is to be respected on the photodetector plane, then the stability of the mirror wall plates has to be such that $\Delta\Theta < 0.05$ mrad for any rotation or deformation of the plates.

8.2 Spherical mirror alignment

The spherical mirrors are mounted on the mirror wall panels. After a time to allow for relaxation of all the mechanical parts, a point source is placed in Cr_i . Mirrors are aligned one by one with respect to this point source. If the point source size is $\sim 100 \mu\text{m}$, then the alignment will be $\Delta\Theta = 0.1/[2 \times 8600] = 6 \mu\text{rad}$, much smaller than the mirror angular resolution, $\Delta\Theta = D_0/[8 \times 8600] = 30 \mu\text{rad}$. D_0 is the diameter of a circle which cover 95% of the reflected light in the focal plane. The whole mirror wall adjustment will also be negligible with respect to the average angular resolution of the mirror wall $\overline{\Delta\Theta} = \overline{D_0}/[8 \times 8600 \times \sqrt{N}] = 7 \mu\text{rad}$. N is the number of mirrors. The obvious disadvantage of this alignment procedure is the need of ~ 9 m clearance in front of the mirror walls. However, its advantages are many: -high precision; -it allows for continuous monitoring of the aligned mirrors, during and after alignment; -therefore, corrections to the initial alignment will be straightforward; -it will allow monitoring for some days or weeks) of environmental effects on the super structure and final testing of critical components; it will provide enough redundancy, to have confidence on the long term stability of the system. A scale prototype is being constructed at the moment, which will test and confirm the procedures here described, apart from being a test bench for the whole optical part of the RICH2.

8.3 Flat mirror alignment

The panels, which host the flat mirrors, will be mounted and roughly aligned to the photodetector plane with the same procedure as above. The point source, previously placed in the centre of curvature Cr_i of the mirror wall, will be placed in a point close, ~ 0.20 m, to the beam axis as in figure 20. The light, reflected by the spherical mirrors, intercepts the flat mirrors and will be focused in a point, common to all mirrors at the photodetector plane. A last alignment of the mirror wall plates can be at this moment applied to comply with the metrology and the eventual readjustment of the flat mirror walls carried out.

When the RICH2 detector is lowered in the pit and placed on the beam axis, this last step will be repeated, to check and correct eventual misalignments. The overall alignment error⁶ foreseen is set solely by the survey (± 1 mm shift on the photodetector plane) and by the precision of the optical mounts. The spherical- and flat- mirror resolution and the mount precision will set the overall resolution of the optical system: $\approx 2.36\sqrt{2 \cdot 0.24^2 + 2 \cdot 0.12^2} = 2.36 \cdot 0.38$ mm at FWHM, where we have considered a $\sigma = 0.03$ mrad precision for each optical component.

9 Monitoring system

During the operation of the RICH2 detector there will be a need to monitor a number of parameters to ensure the quality of the data and the proper operation of all the systems. These were described in the RICH TDR [2] and in an accompanying note [6]. They are summarised here.

9.1 Mirror and photodetector alignment constants

The strategy to be adopted for the determination of the final alignment constants for the mirrors and photodetectors consists on determining the preliminary parameters from the procedure described in section 8, monitor their movements with a laser based system and determine the final constants using data.

⁶It is worth noting the difference between alignment error and optical resolution of the system.

Pressure and temperature variations as well as possible sagging of the mirror supports as a function of time can modify any pre-determined alignment constants in the mirrors. It has been shown [14] that a relative alignment procedure with data tracks can determine the tilts of all the mirror segments to the required accuracy of 0.1 mrad (where alignment effects are negligible) provided that the spherical and flat mirror segments have tilts that do not deviate from their nominal positions by less than 1 mrad. The relative procedure relies on the knowledge of the tilts for at least one mirror segment per detector half. This defines the requirements for monitoring the alignment constants of a few selected mirrors.

It is proposed to perform this monitoring with a laser based alignment system that will deliver collimated beams of light via radiation hard single mode optic fibres at the base of the RICH 2 detector as outlined in figures 21a and 21b. Beam-splitters and mirrors placed outside the acceptance at the bottom and the top of the RICH 2 detector will monitor selected segments of the spherical and flat mirrors. It will deliver two spots of light to the photodetector plane per mirror segment monitored. In this manner, we will be able to distinguish genuine movements of the mirror segment from movements in the alignment system. To allow for redundancy, it is proposed to monitor four mirror segments for each of the two spherical and flat mirror assemblies respectively, a total of 16 fibre and collimator assemblies. A prototype system is currently being built to demonstrate that the required angular accuracy is attainable.

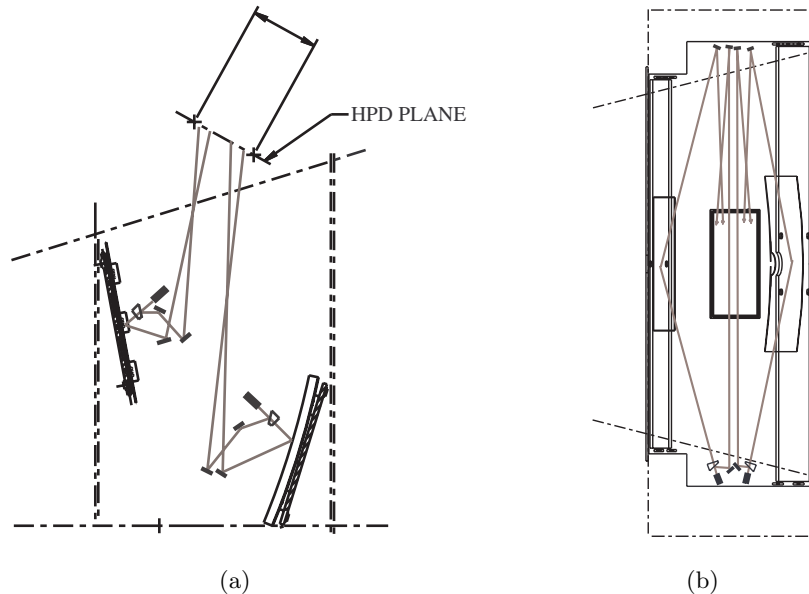


Figure 21: Schematics for a monitoring and alignment system. (a) Top view of the proposed system for monitoring the alignment constants of the mirrors. (b) Side view of the proposed system for monitoring the alignment constants of the mirrors.

9.2 Other monitoring tasks

For completeness, we will also list some other monitoring systems that are needed to successfully run the detector.

- Gas refractive index

The refractive index of the CF_4 gas can be monitored online using a Fabry-Perot interferometer. Details of such a system are described in [15]. This system will allow the refractiv-

ity resolution of the gas to be determined to the required precision: $\Delta(n-1)/(n-1) \sim 10^{-3}$. A prototype system is currently under design.

- **Gas purity**
Purging of the CF_4 gas is achieved with nitrogen gas [16]. To maintain the stability of the refractive index, it is essential to maintain constant the concentration of nitrogen with respect to CF_4 . This concentration can be monitored by using an ultrasound system that measures the velocity of sound in the gas [6]. The velocity of sound v is related to M , the molecular weight of the gas by $v = \sqrt{\gamma RT/M}$, with T the temperature, γ the adiabatic gas constant of the gas and R the ideal gas constant. A demonstration system, using Farnell 400ET 180 and 400ER 180 ultrasound transmitter and receiver transducers operating at 40 kHz, to measure the speed of sound in a column of CF_4 gas admixed with N_2 is currently under construction.
- **Transparency of the gas**
The transparency of the gas can also be monitored with a monochromator through a column of gas of fixed length. A measurement of the absorption spectrum will identify potential impurities in the gas that affect its attenuation.
- **Electronics monitoring**
The high and low voltages of the HPDs and associated electronics, as well as the bias voltages of the silicon sensors and the discriminator thresholds, will be monitored with the use of JTAG controllers by the experimental control system (ECS) [17].
- **Photon detector pixel monitoring**
It is foreseen to install a light pulser inside the RICH2 detector. This pulser will be operated to determine the number of dead or inefficient pixels for all the HPDs.

10 Space requirements

The RICH2 maximum envelope has a minimum clearance along z to the last tracker station of 35 mm and to the first muon station of 20 mm. The minimum distance to the conical vacuum chamber is 45 mm. The detector is in the x direction placed between two support columns which constitute part of the indispensable support mechanics for the calorimeters as indicated in figure 22. The minimum distance to these columns is in the range of about 1 m. We consider these clearances acceptable. The access to a service area for the photon detectors is limited by the mechanics for the electronics of the first muon station as shown in figure 23(2). We anticipate that it will be very rare that we will need to move out a complete photon detector assembly. The access to the electronics is not restricted. This area is at the moment under scrutiny, but we do not see any difficulties in finding solutions which are most satisfactory both for the ease of access to the RICH2 photon detector plane and as well for the electronics of the muon station.

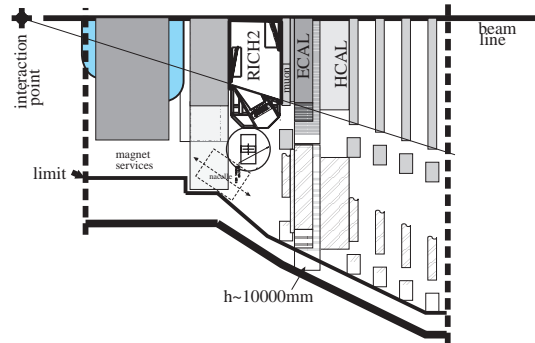


Figure 22: Space configuration around RICH2.

11 Assembly and installation scenario

The assembly of the RICH2 superstructure, chapter 3, will be done in Hall 156 at CERN. The other detector elements are then integrated. The sequence is thought to be as follows:

1. Assembly of the complete superstructure, gas windows and central tube.
 - Gas leak test.
 - Define and survey fiducial marks with respect to floor mounts.
2. Remove entrance and exit windows for safe storage. The central tube is independently supported from its flanges in a \times configuration to the top and the bottom of the superstructure using low mass cables with tension screws positioned outside the acceptance angle.
3. Install rails and magnetic shielding as described in chapter 6.
4. Install rails and photon detector support, chapter 7, and support structure for the monitoring system which is outlined in figure 21.
5. Install mirror panel positioning mechanism and the support panels, chapters 5.6 and 5.5.
6. Install the mirrors and align the optical system as described on page 22.
7. Reinstall entrance window and exit window
8. and the detector is transported to the experimental zone and installed onto pre-surveyed supports.
9. The windows are removed and the alignment of the optical system is verified before the windows are reinstalled.

12 Project organisation

The detector construction and the organisation of the work is unchanged since the RICH TDR. We do not foresee any change in the cost as outlined in the RICH TDR.

Acknowledgements

The LHCb RICH group is greatly indebted to many people at the different collaborating institutes who have with dedication contributed to the various stages from the conception of the detector via the design, testing and prototyping work on which this engineering review is built. We wish to express our gratitude and appreciation to all of them and in particular to M. Alemi, C. Joram, L. Fernandez Hernando, P. Wertelaers and P. Wicht. We are most grateful for the outstanding collaboration with S. Blanchard, G. Foffano and J. Knaster Refolio who have put in an impressive amount of work to study the vacuum chamber and the bake-out scenario around RICH2. Clearly, this engineering work could not have been made without the friendly assistance of the LHCb computing support nor without the LHCb secretarial support.

	Interaction length % of λ_I	Radiation length % of X_0	\pm Horizontal acceptance mrad	\pm Vertical acceptance mrad
Entrance window	0.4	1.0	0 to 300	0 to 290
Exit window	0.5	2.5	0 to 300	0 to 250
Central tube	2×5.0	2×11.5	17.5 to 25.3	17.5 to 25.3
Spherical mirrors	1.4	4.7	0 to 128	0 to 120
Flat mirrors	1.4	4.7	124 to 290	0 to 100
Panels flat mirrors	0.9	3.8	0 to 122	0 to 250
Panels spherical mirrors	0.95	4.0	130 to 280	0 to 250
Support spherical mirrors	0.2	0.5	0 to 128	0 to 120
locally	2.4	6.1		
Support flat mirrors	0.15	0.4	124 to 290	0 to 100
locally	2.0	5.2		

Table 2: Average radiation and interaction length distributed symmetrically in the horizontal and vertical acceptance. Please note that the windows, the spherical mirror panels and the spherical mirrors have circular cut-outs around the central tube.

	mm	Comment
RICH 2 z_{\min}	9450	
Deflection	13	+200 Pa
Tolerance	5	Window thickness, flatness and position
Entrance window	30	1+1 mm carbon fibre/epoxy and 28 mm PMI foam
Tolerance	5	Window thickness, flatness and position
Deflection	4.5	-100 Pa
Clearance	4.5	
RICH 2 z_{\max}	11900	
Deflection	-29	+200 Pa
Tolerance	-5	Window thickness, flatness and position
Exit window	-32	1+1 mm Al and 30 mm PMI foam
Tolerance	-5	Window thickness, flatness and position
Deflection	-11.5	-100 Pa
Clearance	-4.5	

Table 3: The RICH 2 envelope tolerances along z .

Element	Voltage (V)	Number of units	Current (A)
HPD HV lines	20 k	36	$\leq 100 \mu$
Timing, trigger and control (TTC)	3.3	288/2	~ 200 m
Gigabit Optical Link (GOL) chip	2.5	288×2	~ 200 m
HPD pixel chip	3.3	288	~ 510 m
Pixel interface (PINT) chip	3.3	288	
	2.5	288	≤ 100 m

Table 4: On-detector power consumption in RICH 2.

References

- [1] LHCb Technical Proposal, CERN/LHCC 98-4, 28 February 1998.
- [2] LHCb RICH Technical Design Report, CERN/LHCC 2000-0037, LHCb TDR 3, 7 September 2000.
- [3] LHCb Outer Tracker Technical Design Report, CERN/LHCC 2001-024, LHCb TDR 6, 14 September 2001.
- [4] LHCb Moun System Technical Design Report, CERN/LHCC 2001-010, LHCb TDR 4, 28 May 2001.
- [5] G. Hass et al., Reflectance and Preparation of Front Surface Mirrors for Use at Various Angles of Incidence from the Ultraviolet to the Far Infrared, Physics of Thin Films, Vol. 12
- [6] C. D'Ambrosio et al., Monitoring, alignment and control of the LHCb RICH detectors, LHCb 2000-080 RICH.
- [7] C. D'Ambrosio, M. Laub and P. Wertelaers, An experimental set-up to measure the long-term stability of large-mirror supports, LHCb-2000-020
- [8] C. D'Ambrosio, M. Laub, D. Piedigrossi, P. Wertelaers and P. Wicht, Characterization of mirror mount prototypes for RICH detectors, LHCb-2000-072
- [9] The TOSCA Reference Manual, Vector Fields Limited, 24 Bankside, Kidlington, Oxford, OX5 1JE, England.
The TOSCA User Guide, Vector Fields Limited, 24 Bankside, Kidlington, Oxford, OX5 1JE, England.
- [10] Finite Element Analysis, trademarked by: ANSYS Inc., Southpointe, 275 Technology Drive, Canonsburg, PA 15301
- [11] A proposal for a supporting structure for the Hybrid Pixel Detector (HPD) of RICH2, LHCb 2000-82 RICH
- [12] S. Cuneo, M. Ameri, G. Mini, P. Musico, RICH-2 photon detector plane - mechanics to electronics interface, LHCb-2002-010.
- [13] C. D'Ambrosio, L. Fernandez, M. Laub and D. Piedigrossi, The optical systems of LHCb RICHes : a study on the mirror walls and mirrors specifications, LHCb-2000-071
- [14] A. Papanestis, Limits of software compensation for mirror misalignment of the RICH detectors, LHCb-2001-141 RICH. Paper also in the Proceedings of the 7th International Conference on Advanced Technology and Particle Physics, Como, Italy, October 2001.
- [15] M. Sannino, S. Cuneo, M. Ameri, Measurement and monitoring of the refractive index of the RICH gaseous radiators in LHCb, LHCb 2001-145 RICH.
- [16] M. Bosteels et al., LHCb RICH gas system proposal, LHCb-2000-079 RICH.
- [17] LHCb Online System Technical Design Report, CERN/LHCC 2001-40.

13 APPENDIX A

Superstructure. Detailed drawings.

List of figures:

Figure 23

LHCb RICH 2 Superstructure.

(1) Front view of the detector with the entrance window removed.

(2) Horizontal projection of the detector. Also indicated is the position of the muon electronics rack.

(3) 3D drawing of the detector.

Figure 24

LHCb RICH 2 Superstructure.

Side and back view of the detector with the exit window removed.

Figure 25

RICH 2 optical lay-out. See also figure 2.

Figure 26

RICH 2 optical lay-out. Spherical and flat mirror arrangement. See also figure 8.

Figure 27

RICH 2 gas envelope. Horizontal projection. Note the photon funnel ending at the quartz window. The quartz window is detailed in figure 29.

Figure 28

RICH 2 gas envelope. Vertical projection.

Figure 29

RICH 2 quartz window frame assembly.

Figure 30

RICH 2 quartz window and photon detector interface. Photon detector plane in detailed drawings in figures 34, 35 and 36.

Figure 31

RICH 2 window to central tube assembly. See also stress calculations in figure 7.

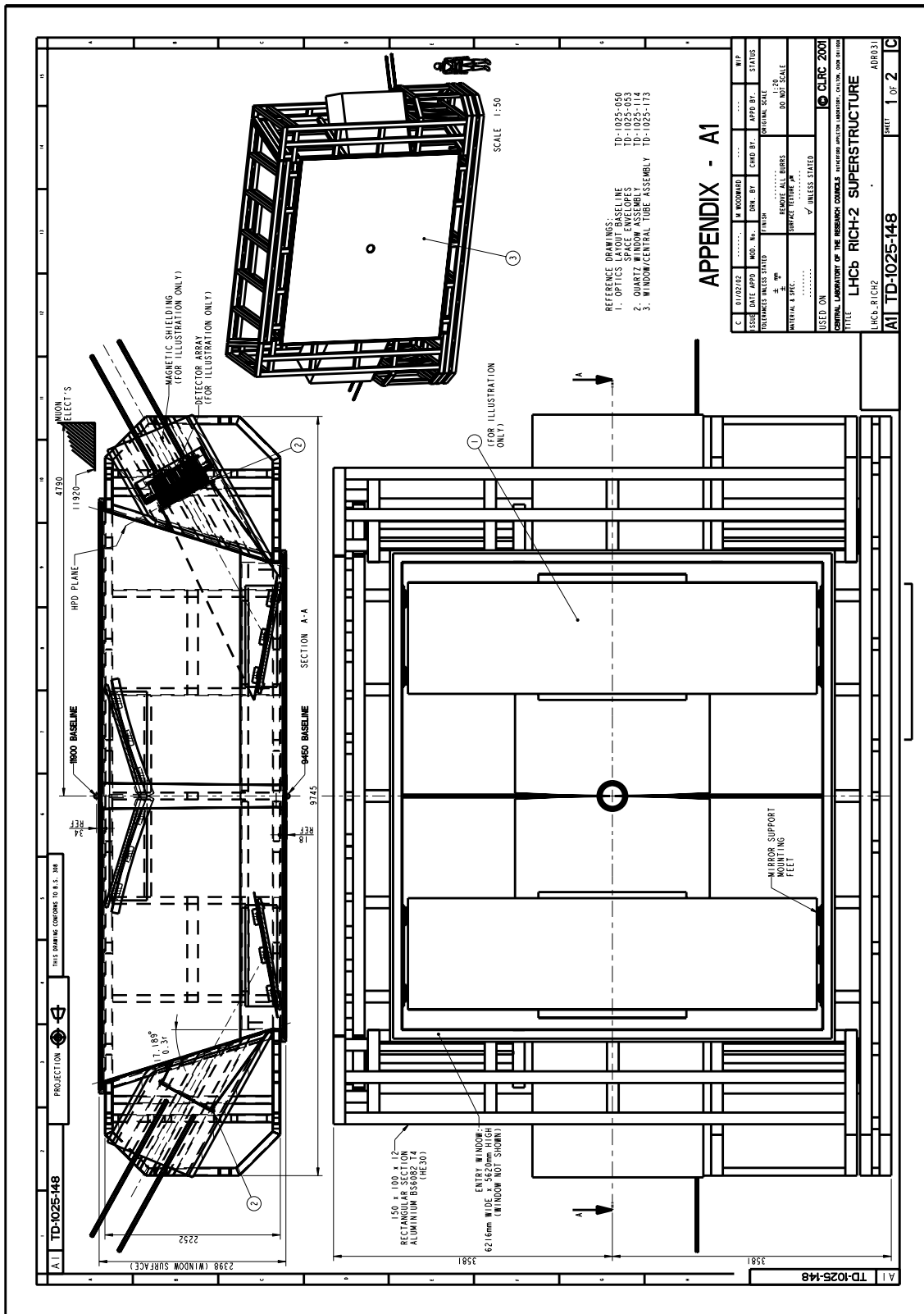


Figure 23: LHCb RICH2 Superstructure. (1) Front view of the detector with the entrance window removed. (2) Horizontal projection of the detector. Also indicated is the position of the muon electronics rack. (3) 3D drawing of the detector.

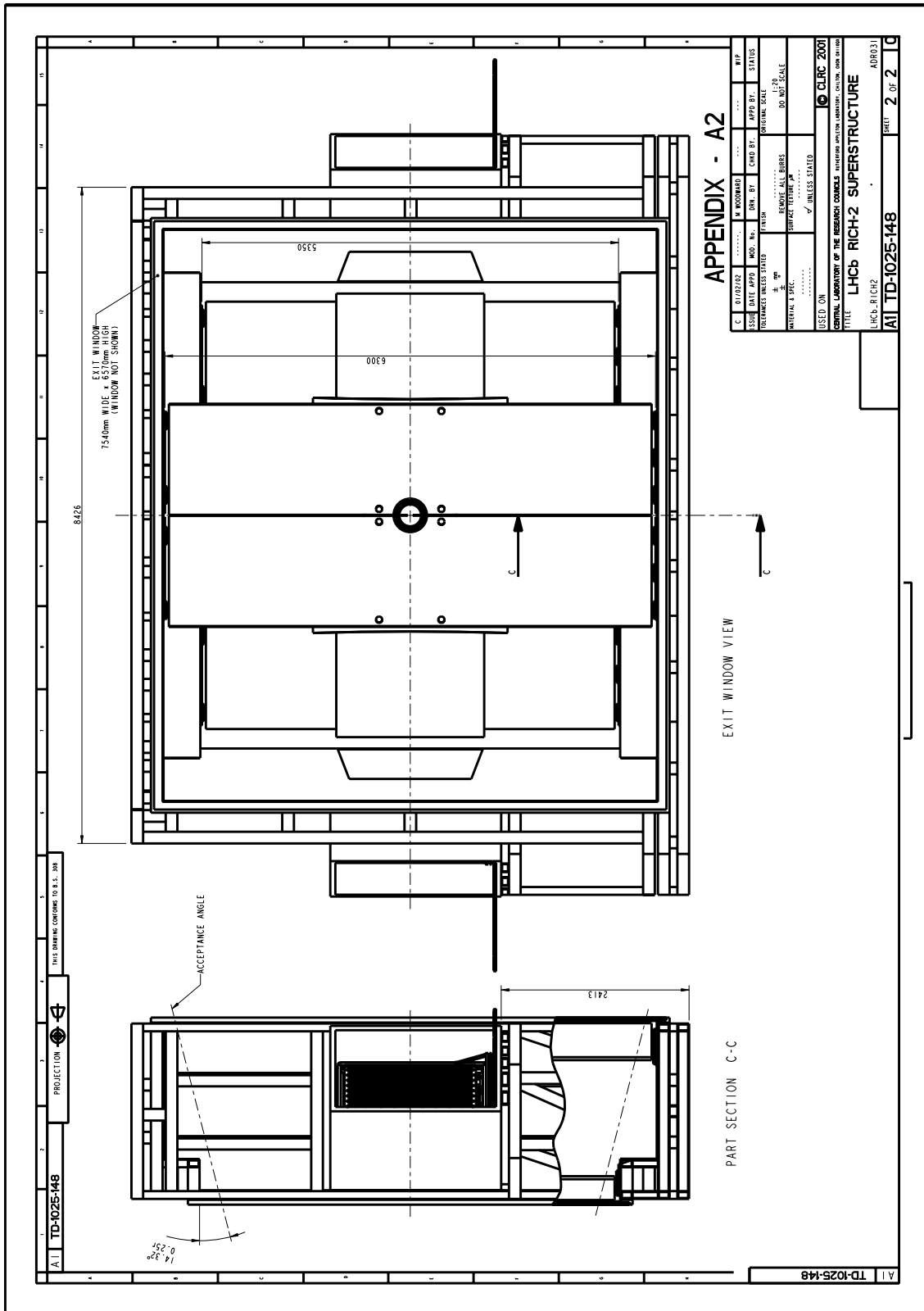


Figure 24: LHCb RICH-2 Superstructure. Side and back view if the detector with the exit window removed.

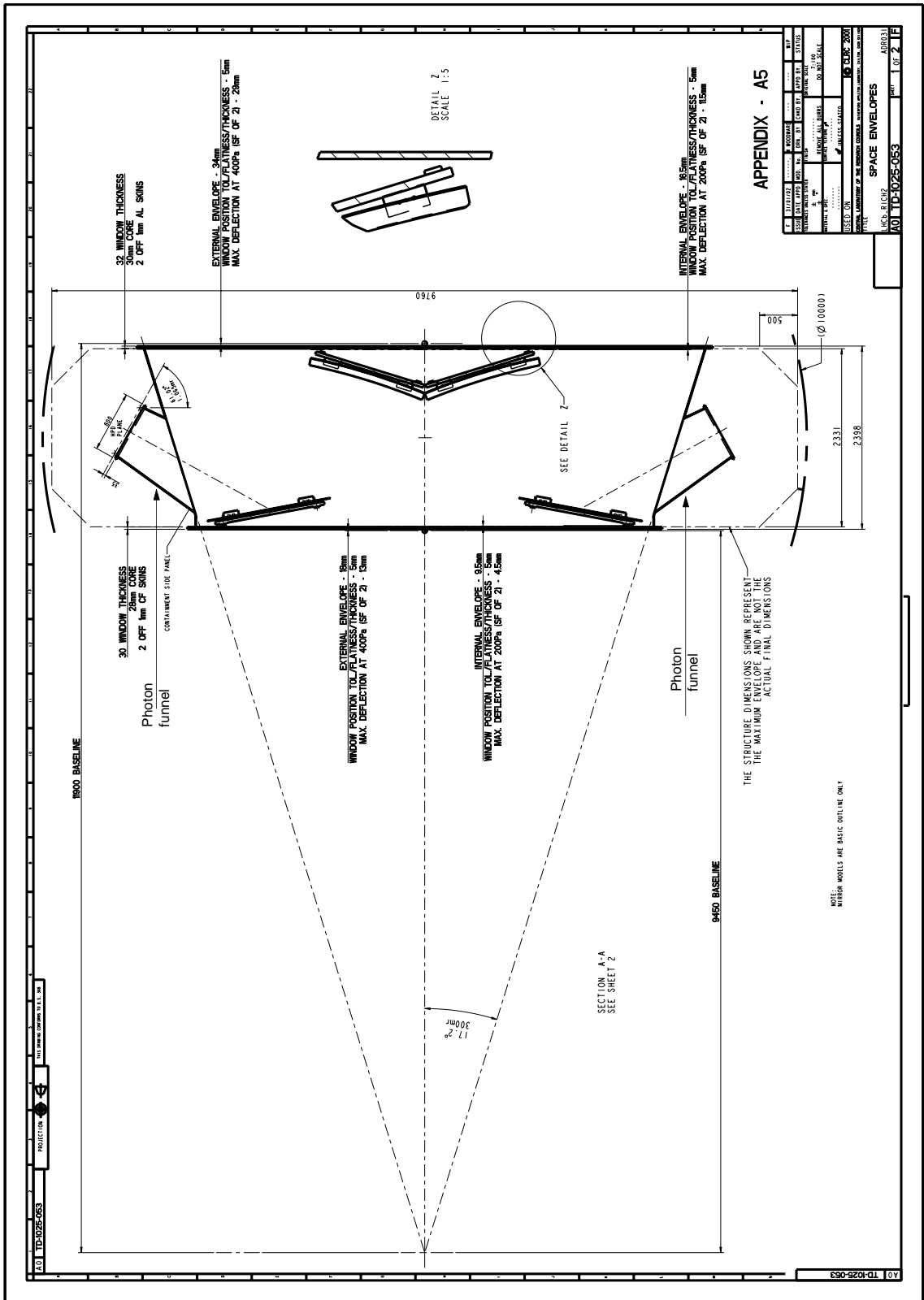


Figure 27: RICH2 gas envelope. Horizontal projection. Note the photon funnel ending at the quartz window. The quartz window is detailed in figure 29.

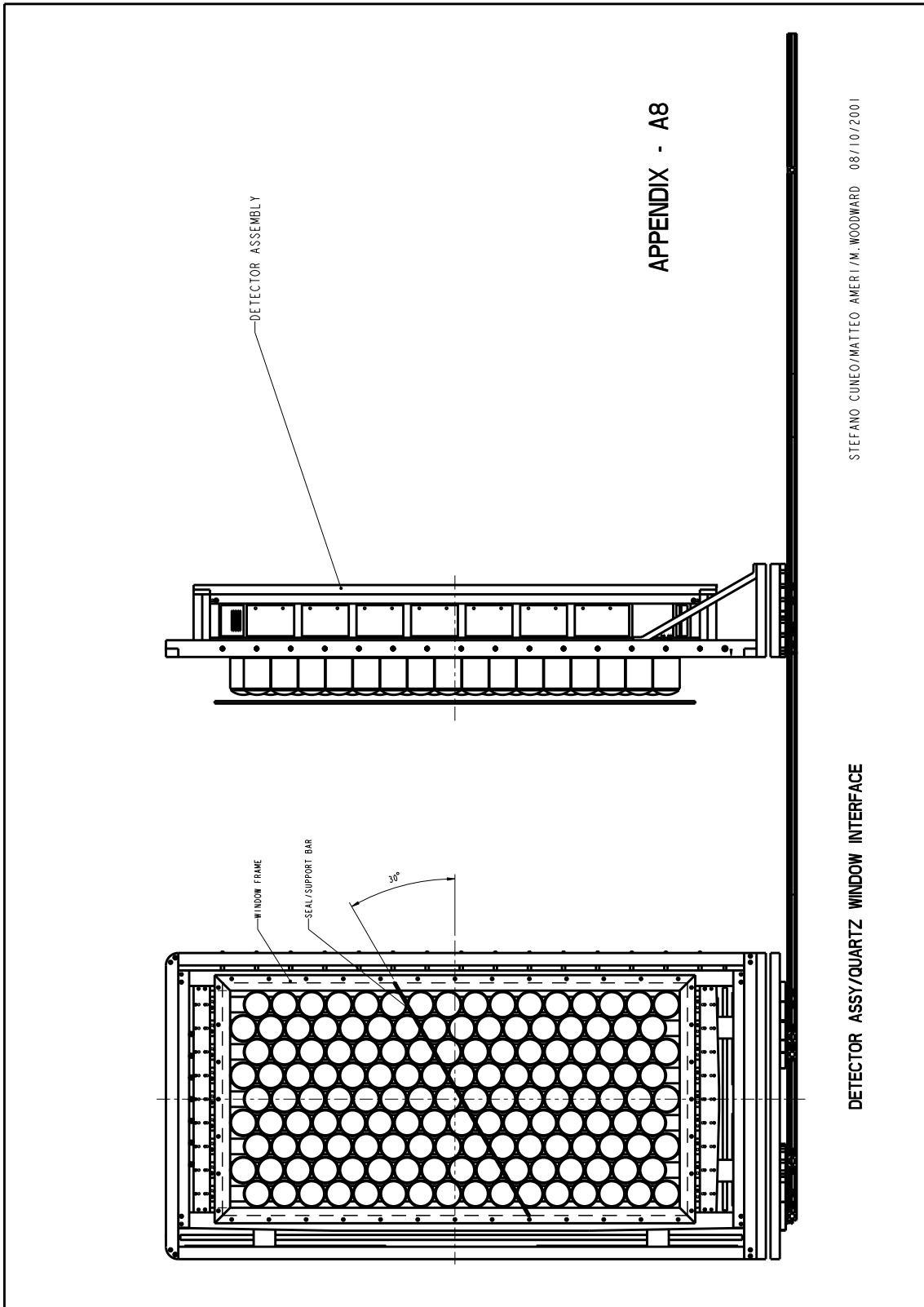


Figure 30: RICH2 quartz window and photon detector interface. Photon detector plane in detailed drawings in figures 34, 35 and 36.

14 APPENDIX B

Photon detector array. Detailed drawings.

List of figures:

Figure 32

RICH 2 photon detector, the HPD, subassembly.

Figure 33

RICH 2 HPD column. See also figure 18.

Figure 34

RICH 2 photon detector read-out assembly. Top view. Left side.

Figure 35

RICH 2 photon detector read-out assembly. Front view. Left side. See also figures 30 and 19.

Figure 36

RICH 2 photon detector read-out assembly. Side view. Left side.

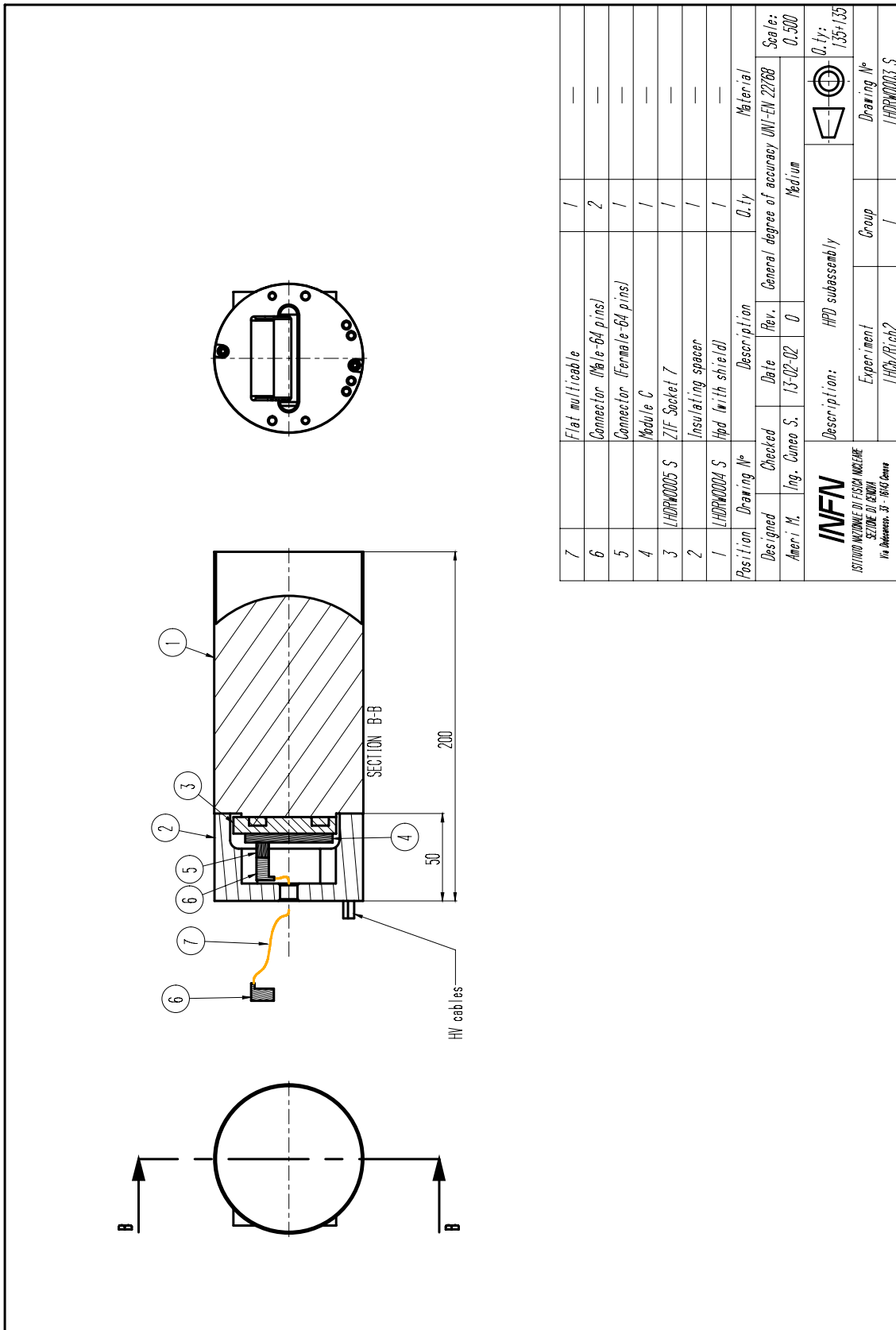


Figure 32: RICH2 photon detector, the HPD, subassembly.

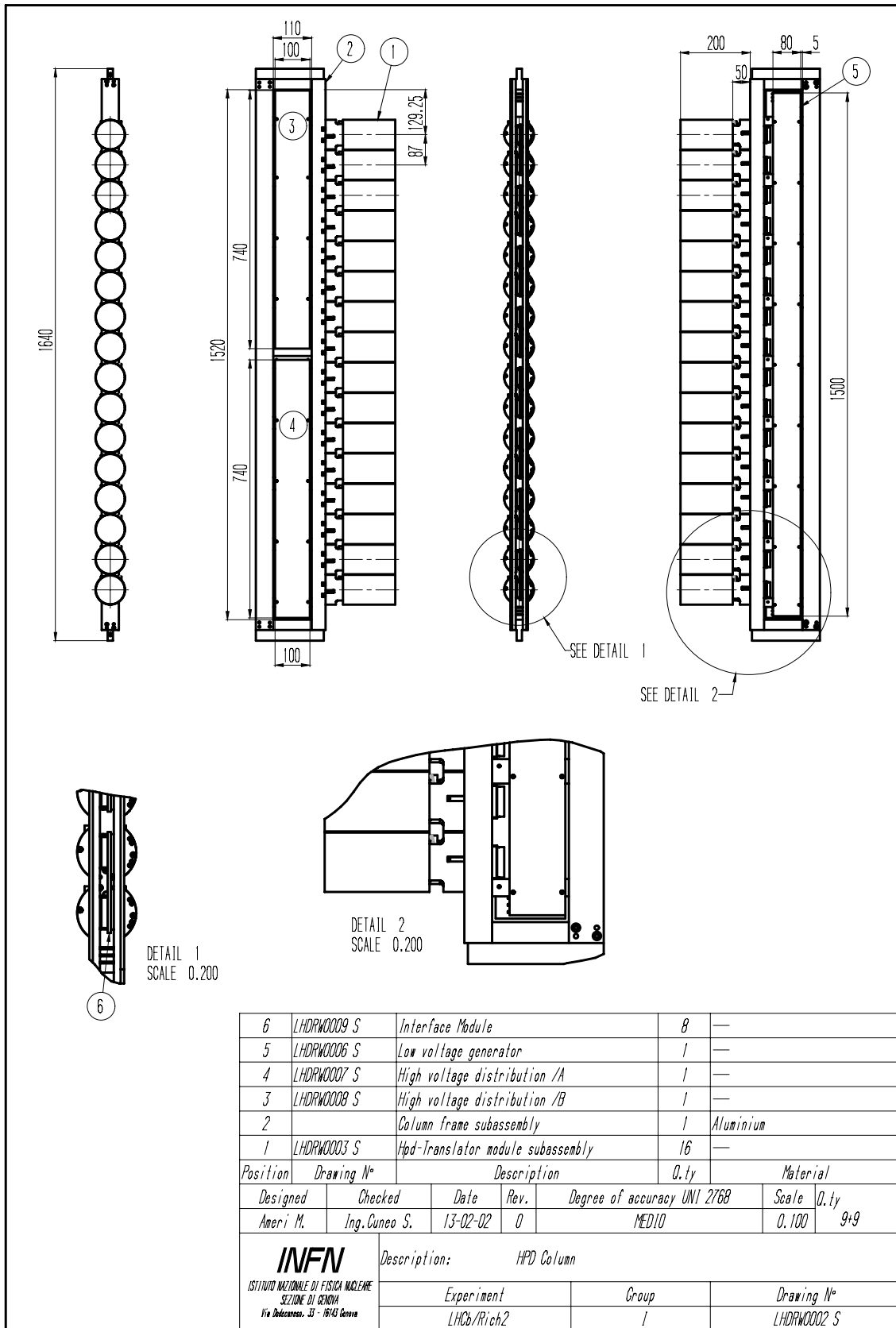


Figure 33: RICH 2 HPD column. See also figure 18.

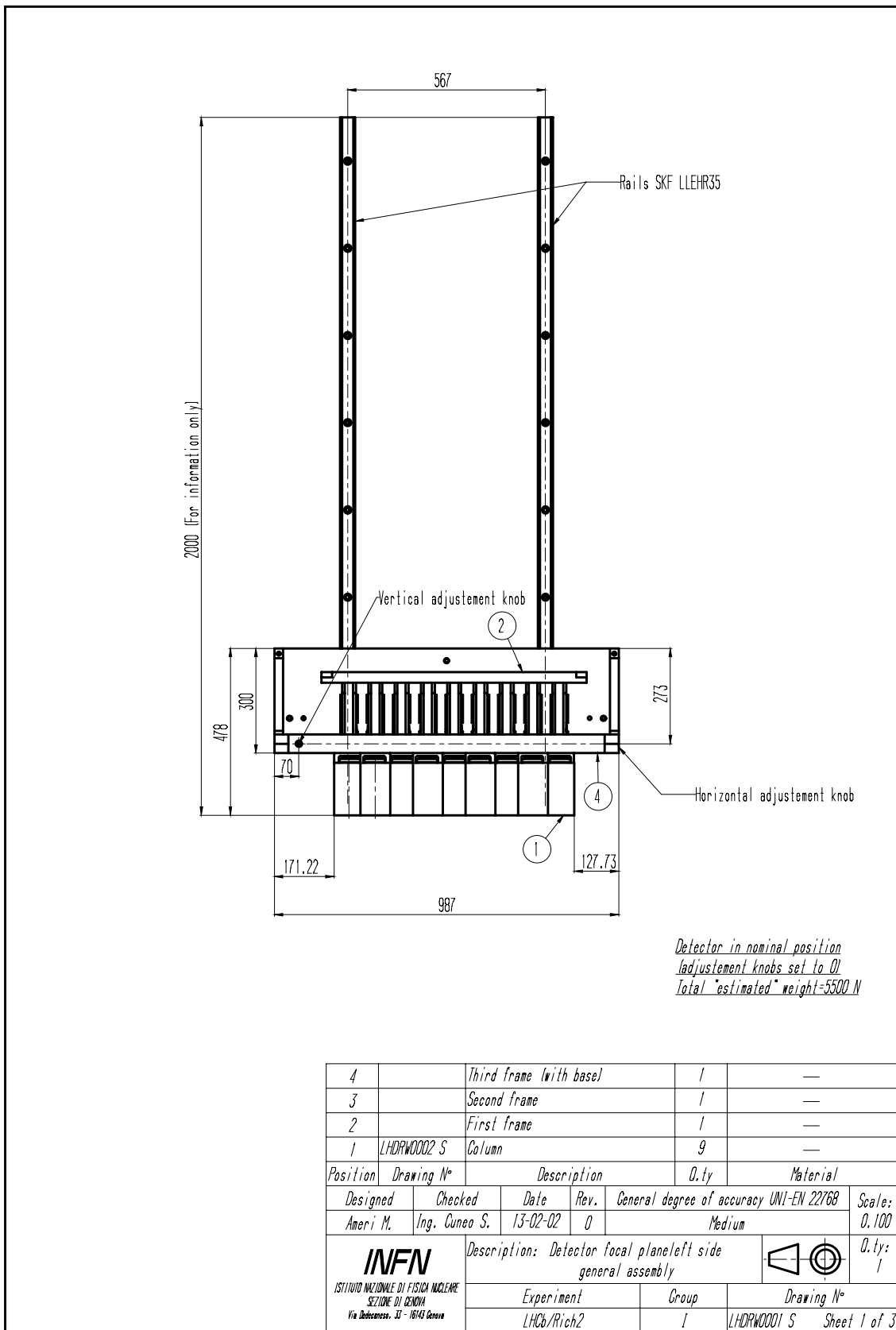


Figure 34: RICH 2 photon detector read-out assembly. Top view. Left side.

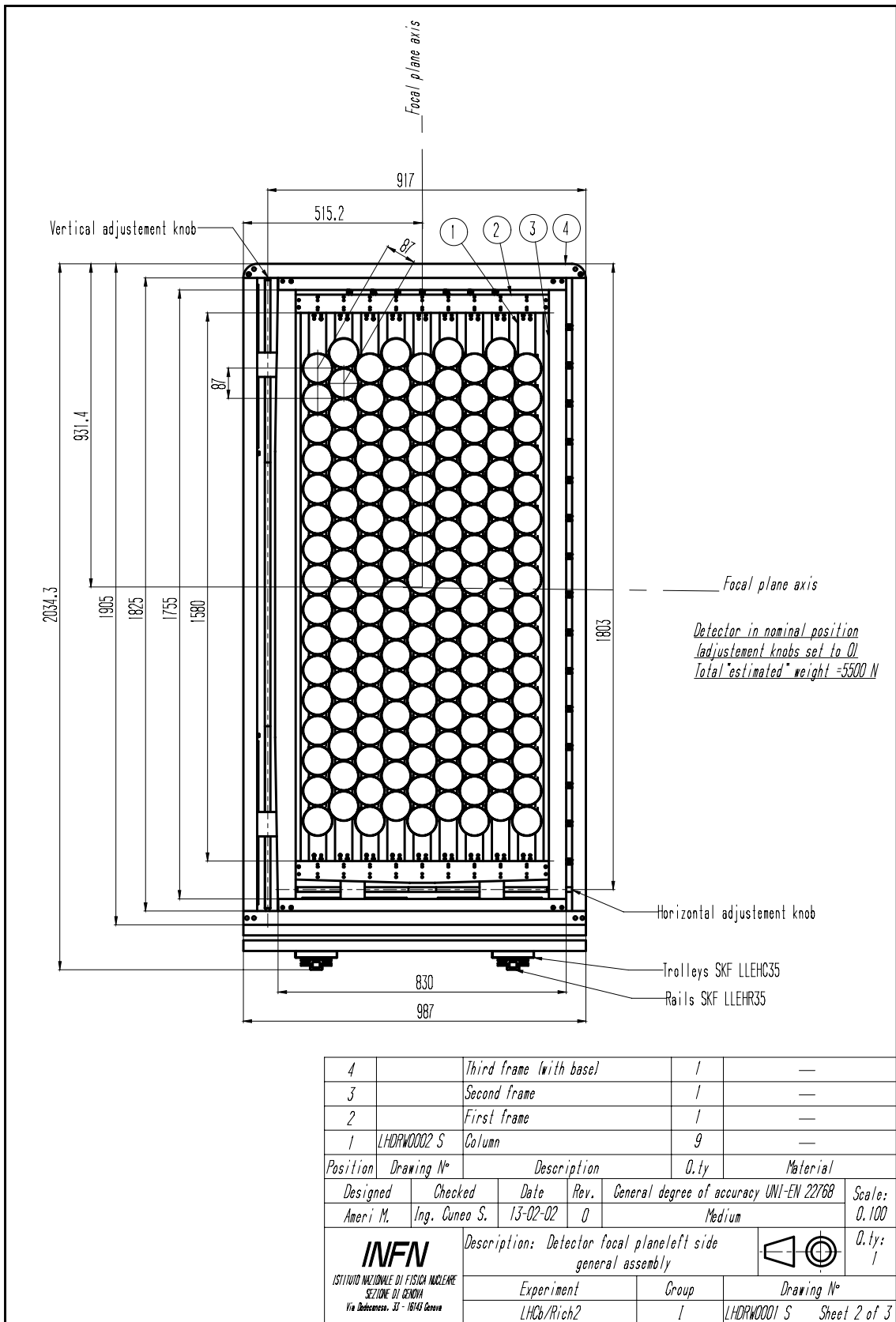
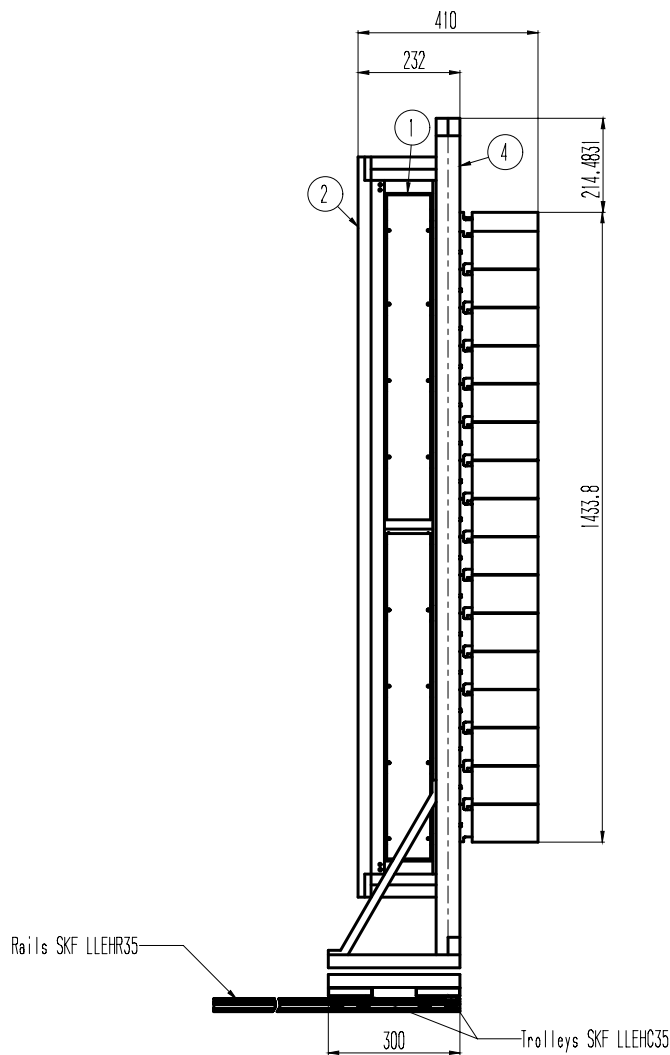


Figure 35: RICH2 photon detector read-out assembly. Front view. Left side. See also figures 30 and 19.



*Detector in nominal position
 (adjustment knobs set to 0)
 Total "estimated" weight=5500 N*



4		Third frame (with base)	1	—	
3		Second frame	1	—	
2		First frame	1	—	
1	LHDRW0002 S	Column	9	—	
Position		Drawing N°	Description	Q.ty	Material
Designed	Checked	Date	Rev.	General degree of accuracy UNI-EN 22768	
Ameri M.	Ing. Cuneo S.	13-02-02	0	Medium	
 ISTITUTO NAZIONALE DI FISICA NUCLEARE SEZIONE DI GENOVA Via Dodecaneso, 33 - 16143 Genova		Description: Detector focal plane left side general assembly			
		Experiment	Group	Drawing N°	
		LHCb/Rich2	1	LHDRW0001 S Sheet 3 of 3	

Figure 36: RICH2 photon detector read-out assembly. Side view. Left side.

LHCb RICH 2 Engineering Design Review Report.

Answers to the referees.

Abstract

The LHCb RICH 2 Engineering Design Review Report was presented 15 March 2002. Martin Doets and Massimiliano Ferro-Luzzi were appointed referees and submitted a first draft Report of the referees dated 20 March 2002. We will in this note give our answers to the comments and the questions formulated by the referees. The comments by the referees are given at the beginning of each section. The answers will follow in more or less chronological order.

1 Co-ordinate system

The co-ordinate system of the LHCb experiment is right handed and the Z-axis is along the proton beam direction. It is worth noting that the angle between the $y = 0$ plane and the horizontal plane is +3.62 mrad. The LHCb RICH 2 detector will be parallel to a vertical/horizontal plane apart from the central tube that will run parallel to the vacuum chamber.

2 Quartz window

- A. *How is the quartz window pair assembled with its stainless steel flange and "I-strip"?*
- B. *Has the difference in thermal expansion coefficients of quartz and stainless steel been considered (for both the "I-strip" and the flange)?*

2.1 Quartz window and the stainless steel flange

The drawing shown in the EDR is a basic concept and shows very little detail. The current proposal is that the \sqcup section shown for the outer frame will consist of an L section and a closing strip screwed onto the L section to form the \sqcup . This will enable the pane assembly to be positioned inside the frame. The quartz panes will be positioned in the I section support strip and located into the L shaped frame using spacers/slips to achieve the various clearances. The assembly will be bonded together using a flexible sealant. Clearances will be calculated to include differential expansion between the quartz and frame components and an allowance for the sealant. The sealant type is being investigated at present with respect to acceptability with CF_4 gas. The closure plates will be screwed in position and the interface between the plates and the quartz filled with sealant. Excess sealant will be removed. The I section will be trapped between the L section and the closure plates and not in slots as shown in the EDR sketch.

2.2 Thermal expansion

The difference in thermal expansion coefficients between the quartz and the Stainless Steel has been taken into account for the current design. Other materials than Stainless Steel are being

investigated. The coefficients are $0.52 \cdot 10^{-6}/^\circ\text{C}$ for HPFS Quartz and $16 \cdot 10^{-6}/^\circ\text{C}$ for Stainless Steel which gives a factor of 30.77 between them. Values for the design temperature excursion of 10°C are given in table 1. The expansion figures are small but we intend to use a flexible sealant in order to reduce stresses on the Quartz window. Some test data exists for this type of sealant.

		Width 750 mm	Thickness 5 mm	Length 1500 mm
Quartz expansion	Top pane mm	$3.9 \cdot 10^{-3}$	$26 \cdot 10^{-6}$	$5.1 \cdot 10^{-3}$
	Bottom pane mm	$3.9 \cdot 10^{-3}$	$26 \cdot 10^{-6}$	$4.9 \cdot 10^{-3}$
Stainless Steel	Frame mm	0.12	$8 \cdot 10^{-4}$	0.24
	Support web mm			$3.2 \cdot 10^{-4}$

Table 1: Values for the expansion for the design temperature excursion of 10°C . The top pane is 987 mm at 60° cut and the bottom pane 943 mm long.

3 Exit/entrance windows and inner tube

- A. *The exit/entrance windows and the inner tube appear to be critical components, since, in case of failure/damage, they require the beam pipe to be removed (a complex intervention with severe LHC/LHCb downtime).*
- B. *What are the limits from the gas system on leak tightness and outgassing of the exit/entrance windows and of the inner tube? (we do not expect them to be severe at all, but we could not find any information on this.)*
- C. *How often will access to the gas volume (venting with air) be necessary? What precautions are taken? What kind of air will be used? How much time is needed for such an operation (gas removal and gas filling)? (Olav's answer: 2 gas fillings $\Rightarrow \sim 2$ days?)*
- D. *Although the radiation dose is expected to be below 100 Gy/year (correct?), could one expect any ageing effects due to radiation for PMI?*
- E. *What are the arguments for not using CF skins for the exit window?*
- F. *Humidity in the gas volume (after some time) should become negligible. Could one expect stresses in the CF window due to the possibly different water content of the inner/outer skins? With respect to water permeability: - Is the used foam a closed-cell foam? - What type of resin is used?*

3.1 Failure scenario

See discussion in section 10.2.

3.2 ROHACELL

General ROHACELL Information⁷: ROHACELL, Polymethacrylimide (PMI) Rigid Foam Sheet, is a closed-cell rigid expanded plastic material for lightweight sandwich construction. It has excellent mechanical properties, high dimensional stability under heat, solvent resistance and, particularly at low temperature, a low thermal conductivity. The strength and moduli values are the highest for any foamed plastic in its density range. ROHACELL is manufactured by hot forming of methacrylic acid/methacrylonitrile copolymer sheets. During foaming this copolymer is converted to polymethacrylimide. The number at the end of ROHACELL represents the density of the foam in kg/m^3 . Some properties are listed in table 2. The water absorption as given in table 2 should be compared to the outgassing property of ROHACELL as given in table 3.

⁷Emkay Plastics, Ltd., www.emkayplastics.co.uk. ROHACELL is a trade name by Röhm GmbH Chemische Fabrik, D-64257 Darmstadt

Tensile Strength, Ultimate	MPa	0.979
Elongation at break	%	3.5
Modulus of Elasticity	GPa	0.0353
Flexural Yield Strength	MPa	0.786
Compressive Yield Strength	MPa	0.393
Shear Modulus	GPa	0.0128
Shear Strength	MPa	0.393
Density	g/cc	0.032
Water Absorption	Equilibrium at 98% RH	19.5%
MAE	15% RH	1.5%
MAE	30% RH	2.9 %
MAE	50% RH	4.7%
MAE	65% RH	6%
WAS	50 days immersion at 20°C	13%
Moisture Expansion Max	50 days immersion at 20°C	1%

Table 2: ROHACELL 31, some mechanical and physical properties. MAE is Moisture Absorption at Equilibrium and WAS is Water Absorption at Saturation.

	Total mass loss %	Recovered mass loss %	Volatile condensable material %
ROHACELL 31	4.98	1.76	0.00
51	5.05	1.92	0.00
71	4.38	1.78	0.00

Table 3: Outgassing property of ROHACELL. Data from ESA MATLAB:3, November: 87.

Even though there could be some shrinkage due to the drying of the foam core, we do not expect any mechanical problem for the windows.

The radiation dose in the LHCb cavern have been calculated with FLUKA99 and is shown in figure 1a for RICH2. The differential spectra at RICH2 are given in figure 1b. The expected dose is therefore ~ 80 Gy/year, ~ 8 kRad/year. Irradiation tests have been performed⁸. The results are given in table 4. Compressive test specimens, $50 \times 50 \times 30$ mm³, and the flexural test specimens, $100 \times 10 \times 10$ mm³, were irradiated with a dose of 0.15 Mrad and 10 Mrad from a cobalt 60 source. There are no significant decrease in the tested properties up to a dose of 0.15 Mrad. The IU Atlas project have conducted tests on ROHACELL 31. They found that at exposures above 9.2 Mrad, the ROHACELL completely gave out and could not hold any more weight. A further test report [3], examines materials including ROHACELL 31-IG using a Cs 137 source with a maximum 20 Mrad dose. The results show that there is a large decrease in ROHACELL properties after 5 Mrad and that below 2 Mrad there is only a 10 % reduction. At 20 Mrad the ROHACELL is brittle, deforms and breaks when handled.

We do not see any danger for the foam core of the windows due to radiation damage.

3.3 Carbon Fibre Composites - Moisture Absorption

Moisture absorption in carbon fibre composites may take place through three routes:

- Along the fibre / matrix interface

⁸Richmond Aircraft Products, www.richmondaircraft.com

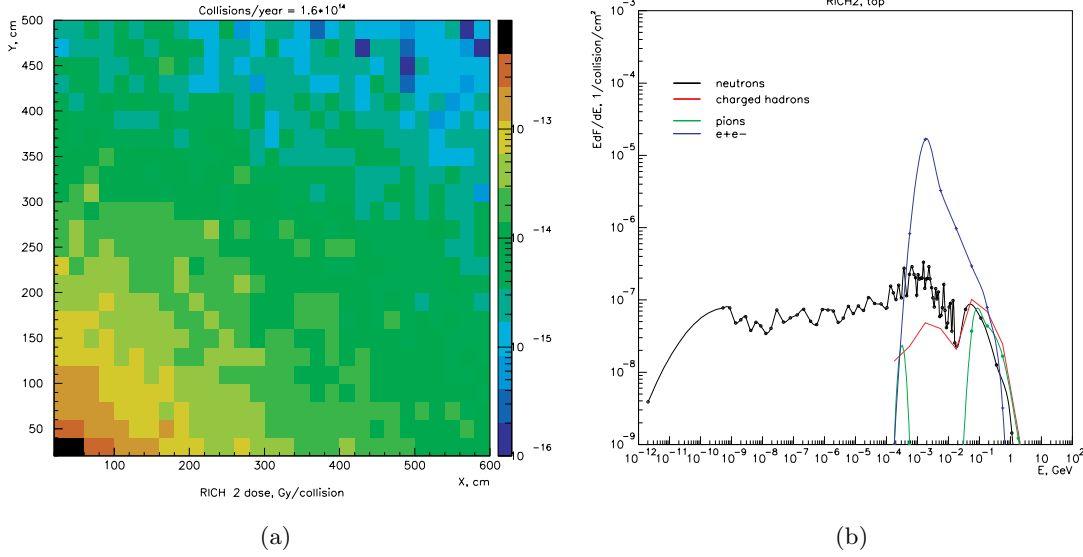


Figure 1: Radiation at RICH2. (a) Radiation dose. (b) The differential spectra. Figures from <http://lhcb-background.web.cern.ch/lhcb-background/Radiation/RadLevels.htm> dated April 11, 2002 .

Compressive Strength N/mm ² (psi)	Flexural strength at N/mm ² (psi)	Deflection fracture mm (in.)	Force at 2 mm deflection N (p)	Exposure
1.5 (213)	2.4 (341)	6.0 (0.24)	11.0 (2.4)	nonirradiated
1.5 (213)	2.3 (329)	5.8 (0.23)	11.2 (2.4)	0.15 Mrad
1.3 (185)	1.8 (285)	2.5 (0.10)	12.0 (2.5)	10 Mrad

Table 4: Mechanical properties of ROHACELL 71 before and after irradiation. Table reproduced from <http://www.phenix.bnl.gov/WWW/publish/bosze/phenixnote272/radiation.html> .

- Through cracks and voids in the composite matrix
- Diffusion through the matrix.

The equilibrium moisture content and associated changes in physical properties of the composite depend on a number of variables, but particularly on the environment, the number of moisture cycles that the composite experiences and on the quality of the composite i.e. the presence of voids and similar defects. It was found [4] that the water uptake of a composite, with T300 fibres, was dependent on the relative humidity and the temperature. At 22 °C, approximately 400 hours was required for equilibrium. The measured weight gain is presented in table 5.

Absorbed moisture swells and plasticises the matrix and since moisture diffusion is not uniform through the material, internal stresses may be present. Absorbed moisture has been found to effect the matrix-dominated properties of composites and has lead to a change in failure mode [5]. An equation was developed [4] for the effect of absorbed water on the swelling of neat epoxide resin, an unreinforced epoxy matrix:

$$\text{Matrix strain} = \frac{1}{3} \times \rho_r \times M_t \times V_L$$

Where M_t is the liquid uptake in g/g of resin, V_L is the volume of absorbed liquid (cm³/g) - (1.0 if liquid is water) and ρ_r is the resin density (g/cm³).

Relative Humidity %	Water Uptake (Weight %)	
	Resin	Composite
45		0.7
75	3.4	1.1
95	5.6	1.6

Table 5: Water uptake as a function of Relative Humidity.

If the water uptake is 5.6 weight %, the associated matrix strain is:

$$\text{Matrix strain} = \frac{1}{3} \times 1.2 \times 0.056 \times 1 = 0.022$$

The translation of resin swelling into laminate strain depends upon fibre orientation etc. However, for a composite based on $\pm 45^\circ$ T300, intermediate modulus, carbon fibres and an epoxy matrix, it was found that the strain is given by:

$$\begin{array}{lll} \varepsilon_1 = 0.0015 & \varepsilon_2 = 0.0024 & \varepsilon_3 = 0.0073 \\ \text{(X direction)} & \text{(Y direction)} & \text{(Z (thickness) direction)} \end{array}$$

Since the fibres are at $\pm 45^\circ$ to both the X and Y directions, it is difficult to understand why the two values are not the same. However, laminate strain in the fibre direction is very small and the windows will have a quasi-isotropic lay up and therefore the laminate strain is expected to be small.

Moisture absorption in epoxy resins results in concentration gradients through the laminate thickness. These gradients result in unequal swelling and therefore stresses and the overall effect is the formation of micro-cracks if the process of water absorption/de-sorption is repeated frequently over a period of time [4]. Conditioning neat epoxy resin and testing at 20°C and 95% relative humidity, resulted in a 20% reduction in Ultimate Tensile Strength, UTS, and $\sim 15\%$ reduction in Young's modulus. For a Uni-Directional, UD, carbon fibre composite where all fibres are at 0° , tested in the transverse direction, (i.e. matrix dependent) the strength was reduced by $\sim 45\%$ after conditioning at 75% RH and by $\sim 60\%$ when conditioned at 95% RH [5]. There was no change in the properties measured in the fibre direction.

The concentration gradients that exist during the process of equilibrating in a humid environment (both sides exposed) were quantified by Sandorff and Tajima [6] and are presented in figure 2. All data on water take up relate to specimens that have been oven dried prior to exposure.

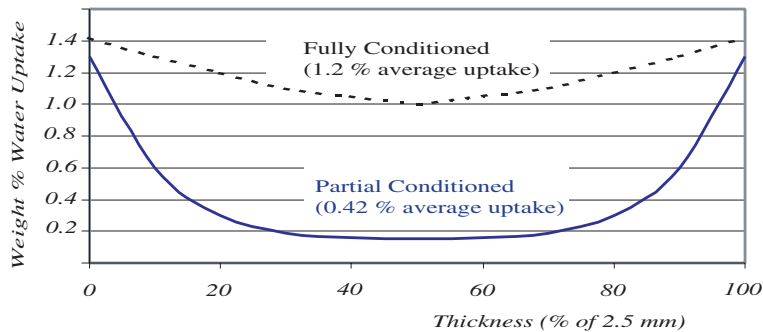


Figure 2: Water Uptake in Epoxy / Carbon Composite [4].

The situation with respect to the RICH 2 windows is that the outer surface of the outer skin will be exposed to the prevailing atmosphere and the inner surface of this skin will see initially, an environment that is similar as found during manufacture of the window. The inner surface of the inner skin will see the manufacturing environment and the outer surface the dry CF_4 gas. Over a period of time there will be tendency for the moisture trapped within the sandwich structure and the inner skin, to migrate into the dry CF_4 gas and for the atmospheric moisture to migrate into the sandwich structure. It is anticipated that equilibrium will be established over a period of many hundreds of hours. Since the situation is not fluctuating, there will not be a cycle in which the moisture content of the skins is changing. There is therefore no reason to believe that long-term damage will result from the effects of water vapour or that there will be significant dimensional changes in the panels as the moisture content changes.

3.4 Leak tightness and outgassing

The mean path length for a Cherenkov photon in RICH 2 is about 5 metres. The gas system for RICH 2 is described in reference [7] and the quantum efficiency for the baseline photon detector, the HPDs [1], is shown in figure 3. The quantum efficiency is peaked around 275 nm. The detection efficiency of the Cherenkov photons is therefore only marginally affected by air contamination. In the figure is plotted the absorption coefficient for water, oxygen and CO_2 . The outgassing from the materials of the gas containing envelope is small. See the discussion in sections 3.4.1 and 3.4.2. The only contamination of the Cherenkov gas which should then be considered, is therefore from air. The leak rate of the complete system is assumed to be in the range of ≤ 20 l/h. The gas system with its inline purifiers, is dimensioned to remove all traces of air to a level of about 100 ppm. The N_2 content will be kept stable at about 1 %.

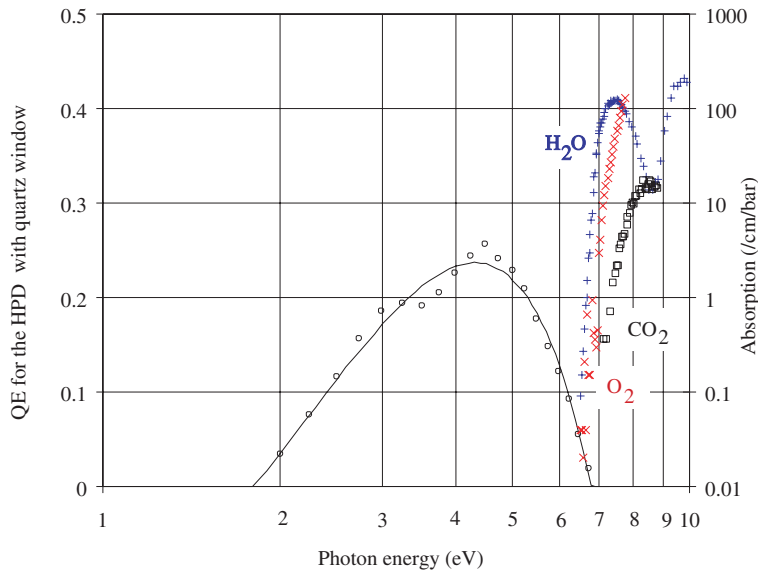


Figure 3: Quantum efficiency of the baseline photon detector, the HPD, plotted together with the photon absorption in water, oxygen and CO_2 , as function of the photon energy.

3.4.1 Limits on tightness and outgassing of the windows

The windows are manufactured from high pressure laminate cured at temperature and will have a low gas permeability. The PMI foam is a closed cell construction. We have no figures for the permeability of air through a composite material. Figures for hydrogen should give a

worse case indication [8]. The permeability of hydrogen gas through a 2 mm thickness of resin based (glass fibre pre-preg) composite material is quoted at a pressure differential of 1 bar as $2.75 \cdot 10^{-11}$ mol/s/m/bar giving a gas transfer rate of $3.3 \cdot 10^{-4}$ ml/s/m². This figure can be applied to both the central tube and the skins of a single window as each total 2 mm thickness.

The carbon fibre skins and foam core assembly is fully bonded into an aluminium frame. An epoxy resin system will be used to bond the skins, foam and frame together. The differential pressure on both the windows and the central tube is +200 Pa/-100 Pa relative to atmospheric. Permeability figures for CF₄ gas through a composite material are not readily available and, if necessary, we could consider arranging the relevant tests. However, the average molecular density of air is 29 g/mol compared with CF₄ at 88 g/mol. It can therefore be argued that the CF₄ atom is larger than an air gas atom and the greater transfer of gases is more likely to be from air into the CF₄.

Using the hydrogen gas permeability figures for the entry window, we get 912 ml/bar, or 1.82 ml/day at 200 Pa

The exit window is manufactured from aluminium alloy, which is bonded together using the same epoxy resin system as the entry window. In this case the length of thickness of a bonded joint is half of an aluminium panel because the panels are overlapped on assembly. Thus we have at least a 500 mm thickness of resin per joint compared to the 2 mm in the entry window skin. The permeability rate will be extremely small and of the order of $1.82/250 = 0.007$ ml/day at 200 Pa.

The above figures are for hydrogen gas and represent the worst case, considering the skins only. The PMI foam is a closed cell structure and will present a large number of thin wall membranes to resist permeation. The foam core is connected in parallel to the skins and any resistance to permeability will serve to further reduce the leakage rate.

A rough estimation of the permeability rates for air with respect to hydrogen can be made from the evaluation of the gas flow through a capillary tube. A simplified relationship [9] is given as

$$q_{pV} = A \frac{d^4}{l} (p_1^2 - p_2^2) + B \frac{d^3}{l} (p_1 - p_2) \quad \text{mbar} \times \text{l} \times \text{s}^{-1}$$

where d is the tube diameter and l is the tube length in cm, p_1 and p_2 the gas pressure at the inlet and the outlet in mbar. A and B are gas dependent constants. For a reasonable set of numbers, this would give

$$\text{H}_2 : \text{He} : \text{air} : \text{R 12 (CCl}_2\text{F}_2) = 1 : 0.64 : 0.37 : 0.32$$

3.4.2 Limits on tightness and outgassing of the central tube

The hydrogen gas transfer rate for the central tube gives 31 ml/day/bar, or 0.14 ml/day at 200 Pa.

The central tube is high temperature cured. An inner Kapton sheet will be added in order to give mechanical protection to the tube from scratches during beam tube bakeout. Kapton gas permeability for 25 μm thick sheet:

Oxygen	3800 ml/m ² /24h/Mpa	at 23 °C and 50 % RH
Nitrogen	910	at 23 °C and 50 % RH
Hydrogen	38,000	at 23 °C and 50 % RH

For hydrogen through the Kapton layer on the inside of the central tube would then give 95000 ml/24h/Mpa, or 19 ml/day at 200 Pa.

The figure shows a higher permeability rate than the composite but this is due to the thickness of 25 μm . At this thickness, although Kapton has good permeability, there is no additional benefit to the composite by bonding the Kapton to the tube. Note that oxygen is a factor of 10 less and nitrogen a factor of 42 less than the above figure.

3.4.3 Carbon fibre window stresses due to water

We are aware that during manufacture there will be moisture take up in both skins and that the window will reach a stable condition of permeability depending on its surroundings. When assembled to RICH2 the inside skin will dry out and stresses may occur. There will also be a second consideration due to the difference between the surface and tunnel humidity on the outside skin.

The carbon fibre panels are a high pressure laminate which is vacuum cured at 65 °C for 9.5 hours and post cured at 120 °C for 2 hours. The peel ply will be removed from the outside surface in order to reduce moisture take up. When bonded to the window frame we will ensure that the carbon fibre panel edges are bonded over and not open to the atmosphere, which will minimise edge ingress. The ROHACELL PMI foam is 100 % closed cell structure and will also be bonded to the carbon fibre skins on both sides and to the aluminium frame at the extremities. The resin system used is two-part epoxy and the mix composition can be varied to suit the curing time necessary for manufacture of the window. We plan to manufacture the windows later this year and we plan to store them carefully in polythene bags to reduce moisture take up with time. The need for a dry gas environment during this storage period needs further investigation.

3.4.4 Carbon Fibre skins for the exit window

The effective track length in the Cherenkov gas has been increased by about 20 % from the TDR [1] to the EDR [2]. This is in part due to the optimisation of the windows. In the TDR, the window material was 48 mm PMI foam with 1 mm glass-fibre reinforced epoxy skins. A $3 \times 3 \text{ m}^2$ test panel has been made. It showed a deflection of 67 mm at 5500 Pa. Reasonable tolerances along z would then be 105 mm for the entrance window and 137.5 mm for the exit window. It was then decided to try to minimise these tolerances and to move the inherent radiation length of the windows closer to the pre-shower detector and at the same time behind the mirrors and the mirror plate. The final tolerances are given in table 3 in [2]. They are 62 mm for the entrance and 87 mm for the exit window, or a gain of 93.5 mm along z for an increase of 0.62 % in X_0 . It is worth noting that the spherical mirrors together with their support, will contribute 9.2 % X_0 . This has to be compared to the radiation length for muon station M1, which has been set to 0.1 X_0 for the chamber sensitive area [10].

Clearly still it would be possible to make the exit window with carbon fibre skins. Inside our limited budget it has been deemed not cost effective. Aluminium alloy skins for the exit window will cost £2000. Carbon fibre skins will cost £33,000.

3.5 Access to the gas volume

It is not assumed that one would need access to the gas volume more than once per year during the winter shut-down. From the experience that we have gained from DELPHI and COMPASS RICHs, the Cherenkov gas will be recovered and replaced by pure N_2 . The nitrogen will then be replaced by dried normal air. Reconstituted air, made up from about 79% N_2 and 21% O_2 , is no longer accepted by CERN safety. The relative humidity of the air is expected to be around 25%. Dust filters will be used at the air intake. The RICH2 gas volume will be

classified as Confined Space as defined by CERN SAFETY CODE A4/Rev. This classification will involve some restrictions to the entering of the volume.

Figure 4 shows a typical recuperation of the C_4F_{10} from the DELPHI Forward RICH system. The vessel was $\sim 2 \text{ m}^3$ and the flow rate of argon was $\sim 100 \text{ l/h}$. Even though there is some mixing of the C_4F_{10} and the argon, the main process is a pure replacement of one gas with the other. The same was true in the replacement of argon with C_4F_{10} . The Cherenkov gas in the LHCb RICH2 is CF_4 . It has a density of 3.88 kg/m^3 . C_4F_{10} has a density of 11.95 kg/m^3 and nitrogen, which will be used as the replacement gas, is 1.25 kg/m^3 . We would therefore expect a somewhat higher mixing ratio between the Cherenkov gas and the replacement gas than in the DELPHI Forward RICH case. 2-3 volume changes should be sufficient. During normal operation, the gas flow rate per hour will be close to 10 % of the total gas volume [1]. The flow rate is expected to be higher during emptying and filling. 24 h should therefore be sufficient for each of these operations.

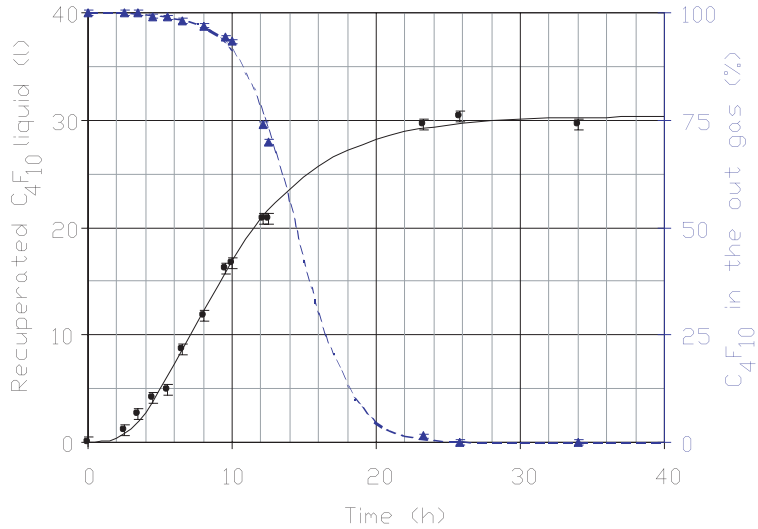


Figure 4: Recuperation of the C_4F_{10} in the DELPHI Forward RICH. The percentage of C_4F_{10} in the out-put gas from the vessel, the right hand scale, is measured with a sonar.

4 The mirror panels

- A. The natural frequencies of the sandwich panels were calculated to be 2, 10, 12 Hz, ... (and similar numbers can be found in the TDR for the RICH2 structure: 1.2, 1.4, 2.9 Hz). A plot of the cavern noise spectrum was shown with a large peak at 1 Hz. It was not clear to us what conclusions were drawn from this comparison.
- B. Has CF been considered for these panels? (stiffer and lighter, but then thermal expansion coefficient must be considered)
- C. The option of pulling the sandwich panels at the top (with a spring) should be kept.
- D. Is a reinforcement at the bolts (B) in Fig. 12 of Ref. [1] not needed?

4.1 Vibrations in the experimental cavern

Results of seismic vibration measurements in the LEP tunnel are published in reference [11]. The Power Spectral Density is defined as

$$P(f) = 2 \cdot \lim_{T \rightarrow \infty} \frac{1}{T} |q(f)|^2 \quad \text{where} \quad q(f) = \int_{-T/2}^{T/2} x(t) \cdot e^{-i\omega t} dt$$

The measured variable $x(t)$ is a velocity and $P(f)$ is defined as Velocity Power Spectrum Density, PSD_v , with the unit $(\mu\text{m/s})^2/\text{Hz}$. The associated Displacement Power Spectral Density, PSD_d , has the unit $\mu\text{m}^2/\text{Hz}$ and is defined as $PSD_d \equiv PSD_v/\omega^2$ where ω is the local circular frequency. The total RMS displacement is given by

$$Z_{RMS} = \sqrt{\int_0^{\infty} PSD_d(f)df}$$

The contributions from the various frequencies can be determined by integrating the spectrum from $-\infty$ or f_{max} to the frequency of interest.

$$I(f) = \sqrt{\int_f^{f_{max}} PSD_d(f)df}$$

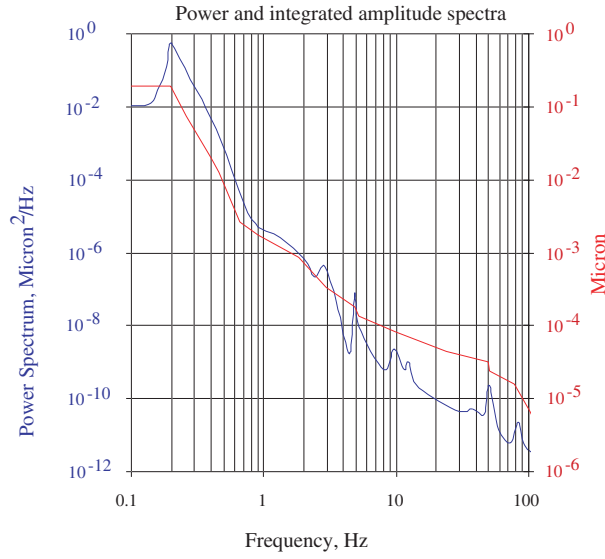


Figure 5: Power and integrated power spectra of vertical vibrations measured in quiet conditions. CERN TT2A tunnel [11].

Power and integrated power spectra of vertical vibrations are plotted in figure 5. A power spectra has also been taken in the LEP Pit 8 during DELPHI operation to verify possible noise enhancement from cryogenic compressors. We are currently analysing these data. They are however very similar to the general seismic noise behaviour in the CERN machine tunnels. We would therefore not expect any problem with the RICH2 structure, nor for any component in it, from seismic vibrations.

Even though in general terms, a higher natural frequency for the object would indicate a higher stiffness, inspection of figure 5 does not reveal any peaks in the power spectra which should be avoided. The change in the design of the superstructure from Stainless Steel I beams to closed profile aluminium beams, together with other design changes, changed the first natural frequency from 1.2 Hz to 12.3 Hz. The corresponding one for the mirror sandwich panel is 2 Hz. The first natural frequency for a composite beam of length l under uniform load, is given as

$$f_1 = \frac{\pi^2}{2\pi} \sqrt{\frac{EI_{\text{pan}}}{ml^4}} \quad , \quad I_{\text{pan}} = \frac{th^2b}{2(1-v^2)}$$

where E is Young's module, v is the Poisson ratio, h is the height and b is the width of the beam, t is the skin thickness and m is the linear mass. As most of the variables for the mirror sandwich

panel are given by construction, we have very little freedom to change the natural frequency. The choice of the material is discussed in chapter 4.2. The stability measurements on the full scale panel prototype will show if there are some particular effects due to this phenomenon. This test will be carried out in a hall which is less stable than the final experimental area.

A further study has been done on possible vibrations induced by sound pressure. Figure 6a shows the vibrational output power of a fairly large air-conditioner. The rotational frequency of the fan was 890 rpm and the fundamental mode of vibration was 14.8 Hz. The several frequency peaks originated from this fundamental mode can be seen in the same figure.

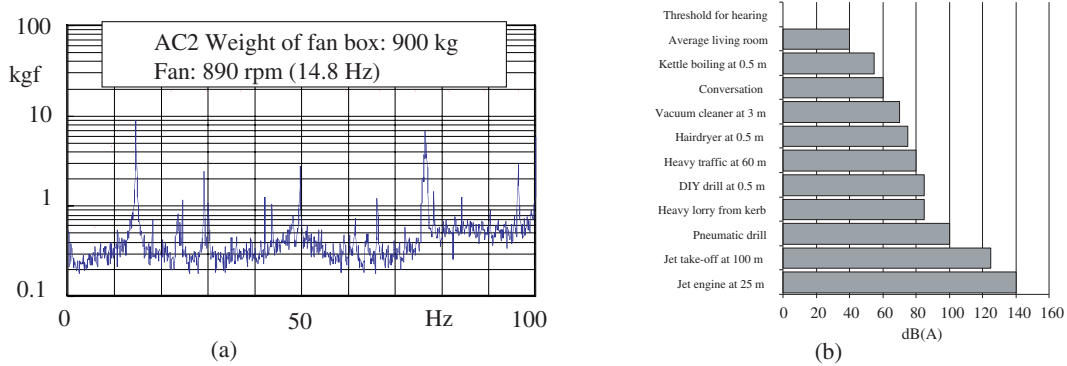


Figure 6: (a) The output power spectrum of the air-conditioner No.2(AC2) [12]. (b) Some everyday noise classified in $\text{dB}_{\text{acoustic}}$.

Acoustic noise is defined as

$$dB_{\text{acoustic}} = 10 \cdot \log_{10} \left(\frac{p_1}{p_0} \right)^2 \quad \text{where } p_0 = 20 \mu\text{Pa} \quad \text{or} \quad 100 \text{ dB} = 2 \text{ N/m}^2$$

Figure 6b shows some noise sources classified in $\text{dB}_{\text{acoustic}}$. The sound absorption through a foam composite is approximately zero for frequencies below 100 Hz. By assuming a realistic noise level at RICH 2 at around 80 to 90 dB, this would give a z excursion for the mirror plate in the range of $\ll 10 \mu\text{m}$. This is a perturbation small enough to be neglected.

4.2 Carbon Fibre skin

The single photon resolution required for RICH 2 is about one order of magnitude better than what have been achieved so far for large detectors. It has been observed that composite plastic materials in contact with fluorocarbons will either swell or shrink. Furthermore, it has been observed that plastifiers that have been added in these materials could be washed out [13]. An example is given in figure 7. Composite plastic materials have therefore been avoided for the crucial optical components. Aluminium sandwich panels have been chosen. Metallic material will limit considerably creep compared to polymer material. A metallic material is less sensitive to conditions such humidity, outgassing, and radiation. The aluminium skins are easy to machine and they allow to fix precisely the mirror support without local reinforcement. The price of aluminium sheets and the panels manufacturing will be less compare to the carbon fibre prepreg.

4.3 The vertical pull on the mirror panels

As the panel stiffness is quite high, no buckling is expected. The pulling mechanism will be kept on the full scale prototype and the usefulness of it will be verified.

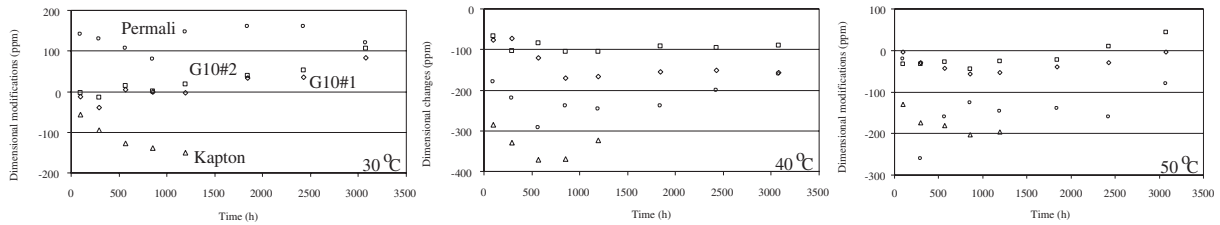


Figure 7: Dimensional modifications as function of time and of temperature of the C_6F_{14} liquid. The samples are G10#1: ISOLA type glass fibre reinforced epoxy 10 mm thick. G10#2: ISOLA type glass fibre reinforced epoxy 20 mm thick. Kapton: 125 μm thick polyimide. Permalloy: Permalloy type glass fibre reinforced epoxy 4 mm thick. Plots reproduced from [13]. The measurements are done at room temperature and the ageing at the temperature given in the plot.

4.4 Local reinforcement of the mirror panels

Comparison of stability has been done between samples with and without inserts embedded in the sandwich panel. These tests were carried out with a mirror support similar to the design showed in the TDR [1]. No clear difference of the relaxation behaviour between these two configurations could be established. As the new design of the mirror support as presented in the EDR, the regions where the mirror supports will be fixed on the panels will be less weakened than by the big holes needed for the previous design. The benefit of inserts in order to locally reinforce the panel, should therefore not be required.

5 Mirror support

A. *Could one expect any ageing effects due to radiation for Polycarbonate?*

5.1 Radiation induced ageing

The radiation dose at RICH 2 is shown in figure 1a. The expected dose is ~ 80 Gy/year. General relative radiation effects on thermoplastic resins are given in figure 8. The useful operating limit for Polycarbonate is in this reference given as $\leq 2 \cdot 10^4$ Gy with a possible extension up to $\sim 10^6$ Gy.

6 Magnetic shielding

- A. *Although a rough calculation of the B-field inside the shielding box versus shield thickness was carried out with ANSYS prior to running the full TOSCA simulation, we recommend to confirm that the choice of a 60 mm wall is appropriate (and not an overkill) by making 1 or 2 more full simulations with a thinner shield (down to about 40 mm).*
- B. *Typically, mu-metals become useless when they are exposed to excessive magnetic fields. What is "excessive" in the case of the photon detectors mu-metal shields? In the RICH TDR (p. 54) it is said that the shielding cylinders are "an integral part of the HPD". What does this mean exactly? Are they easily exchangeable? What has been foreseen to ensure that these shields are never exposed to such magnetic fields (e.g. during installation or interventions)? How critical is this (in case of a mishap)? Will the LHCb magnet be always be switched off during interventions? Will there be an interlock? (if needed)*

6.1 Thickness of the overall magnetic shielding

A new complete simulation of the overall magnetic shielding together with the simulation of the stray field from the magnet has been done. The 3D computations done for the shielding box with thickness of 60 and 45 mm do not give much difference in terms of magnetic field

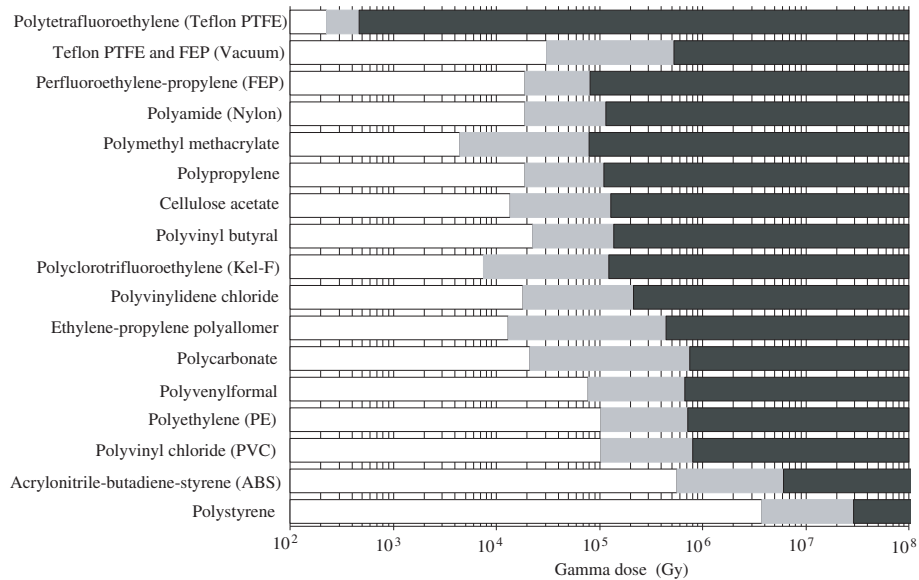


Figure 8: General relative radiation effects: Thermoplastic resin. White: Damage; Incipient to mild, Utility; nearly always usable. Grey: Damage; mild to moderate, Utility; often satisfactory. Black: Damage; moderate to severe, Utility; not recommended. Atmospheric and other environmental conditions such as dose rate are not taken into consideration. Plot from [14].

attenuation. On the other hand, for the 30 mm thickness box, there is a visible reduction of the surface inside the shield where the field is limited to 5 Gauss as shown in figure 9. For the 30 mm thickness the force acting on the single shield is about 2 kN towards the origin. It is about 1/3 of the value for the original 60 mm thickness.

It should be noted that the final B-field configuration of the LHCb experiment will not be known with certainty before the experiment is installed together with the hadron calorimeter and the muon filters. The magnetic field at the photon detector plane will be verified when RICH2 is installed on the beam line. The overall magnetic shielding structure does not lend itself easily to changes nor to upgrades in case it should prove indispensable. It has therefore been our working hypothesis to over-dimension the shielding structure rather than minimising the weight. The superstructure is designed to support the current design and there is fairly little money to be gained in saving some weight as the main cost is in the manufacturing of the structure.

The design philosophy of the magnetic shielding structure has changed from the TDR to the EDR. The TDR design was a very open structure with a large clearance around the photon detector structure. This was a luxury that we could not sustain. The new design is a more minimalist design where all clearances have been cut down to the near minimum. The length behind the photon detectors have been kept in order to not have a closing iron plate. The shielding structure design is such that if required, this plate can be installed.

Before the final TDR design, 4 different models were studied [15]. The characteristics of these models are given in table 6. The result of the last model was verified with a scaled structure. From these simulations it is clear that 3 cm are not sufficient and that the shape plays a role in the stability of the solution.

6.2 Mumetal shields

A simplified matrix of Mumetal shields have been simulated inside an iron box structure [16]. The far magnetic field is 100 Gauss vertical and the shield cross section is rectangular with a

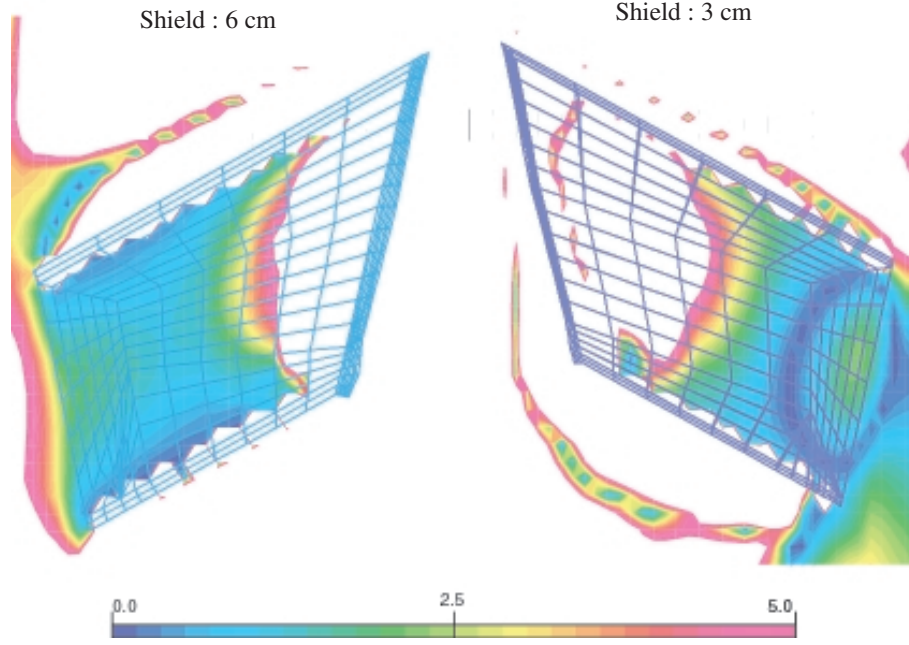


Figure 9: Magnetic field configuration for the overall magnetic shielding with an iron thickness of 6 cm, left side, and 3 cm, right side. The plot is in the plane $y = 0$.

# of layers	Thickness of layers (cm)	Interspace (cm)	Comment	Calculated B-field at detector plane (gauss)
2	1.5	10		7.5 to 24
3	4	4	smoothed angles +1 m along z	3 to 23
3	4	4	as above + front wall	3 to 20
3	4	4	as above + house shaped	2 to 8

Table 6: Characteristics of models for the overall magnetic shielding for the TDR [15].

1 mm thickness. It has been verified that the latter approximation does not change significantly the results. The effect of the local shields are to reduce the external magnetic field to a marginal value inside the HPDs. The shields do not significantly disturb the field distribution inside the overall magnetic shielding. The magnetic field values within the Mumetal itself, is far from the saturation level of 0.7 Tesla. The maximum of this value occurs for the central shields and it is around 0.3 Tesla. The presence of the shields have the effect of slightly attracting some magnetic flux lines at the top and the bottom of the columns. There is a decrease at the middle of the column. See figure 10.

A comprehensive integration study of the HPD body, cabling and the local magnetic shielding together with the detector mounting has not yet been terminated as we still need some further understanding of the tolerances and constraints involved. For the EDR, we have therefore taken the option to consider the HPD with its Mumetal shield as one entity. The shield could be glued onto the HPD base. We do not at the moment see any reason for an easy exchange of shields.

Mumetal material can work efficiently to attenuate the magnetic field up to an exposure

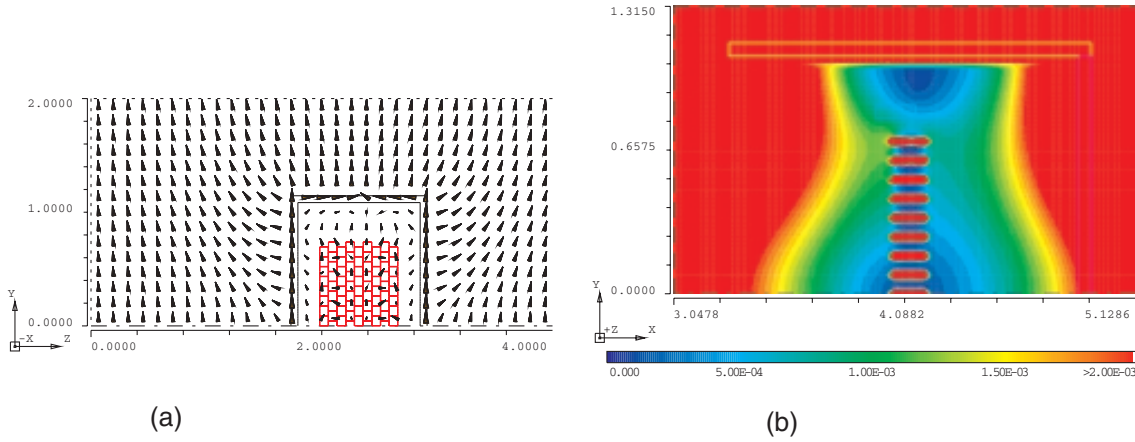


Figure 10: B-field distribution in the model [16]. The co-ordinate units are in meters in a local co-ordinate system. (a) is showing the far field, the effect of the overall magnetic shielding and the matrix of Mumetal shields of a vertical cut parallel to the HPD photon cathode through the middle of the HPD matrix. The arrows show in logarithmic scale the B field distribution. (b) shows the magnetic field amplitude in a vertical cut along the axis of the HPDs for one edge column.

which corresponds to the level of the saturation for the material. This can be referred as the excessive magnetic field. However, there are no hysteresis effect, and when the field is switched off, the Mumetal goes back reversibly to the original condition and it can be successfully used again to operate as a shield, no matter which was its past history in a magnetic field. Possible exposure of Mumetal shields to magnetic field higher than its saturation value is not a problem.

The photon detectors will not be removed from the overall magnetic shielding structure when the magnet is on and interlocks will be installed.

7 Photon detector mounting

- A. *In view of the fragility and weight of a populated column, it seems that a handling device is needed. The tooling needed for removing a single column should be clarified.*
- B. *What are the requirements on stiffness of the column frame?*

7.1 Single column handling device

It is not foreseen to disengage a single column from the structure when the structure is in its base position. Most of the on-detector electronics could be reached in this position. Intervention on a photon detector or on a single column can only be foreseen when the structure has been slid out of the overall magnetic shielding structure. Only at that time could a column be first disconnected, then disengaged and finally extracted while sliding on the guides foreseen on the global frame. When a large enough length of the column frame protrudes from the global frame, it would be supported by means of ropes. Such ropes could easily embrace the upper beam of the frame, as shown in the column assembly drawings. A small lifting device could be useful to ease the manipulation of a column. It could be integrated in the superstructure.

7.2 Stiffness requirements of the column frame

The column is meant to be handled and operated always in vertical position. A preliminary modal analysis of the column found the first frequency at 45 Hz. This indicates that the stiffness is high enough to withstand even accidental loads due to inclinations of the photon detector plane

assembly during transportation. Vibration damping through global structure foundations should be foreseen.

8 Alignment and monitoring

A. *What is the time needed for the alignment of all optical components?*

B. *How do possible cavern floor movements affect the RICH2 performance?*

8.1 Time requirements for alignment

From our experience with the COMPASS RICH detector, we would estimate that about 6 to 8 mirrors can be aligned in one day. The LHCb RICH2 has 96 mirrors. This work is foreseen to be done in Hall 156 and we do not foresee any time pressure. The alignment checks that will take place in the experimental cavern, should take about one week. This last item has to be carefully scheduled as it might require restrictions to other work in the area.

8.2 Movement of the cavern floor

The experimental cavern, together with the rest of the LHC installation, is floating in the molasse and the moraine. The exact position and size will change as a function of the earth tides as shown in figure 11, the variation of the height of Lac Léman and similar geological phenomena. More information can be found in [17] and [18]. These effects are small and did not give rise to any problem for the local alignment of the experiments at LEP. There was though, a measurable effect on the energy delivered by the LEP machine. We would expect that as at LEP, the experiment is internally realigned after each winter shut-down.

The influence of seismic vibrations on the RICH 2 structure is discussed in section 4.1. We have here not addressed more violent earth movements like earthquakes, as we consider these events to be rare and traumatic for the experiment as an entity.

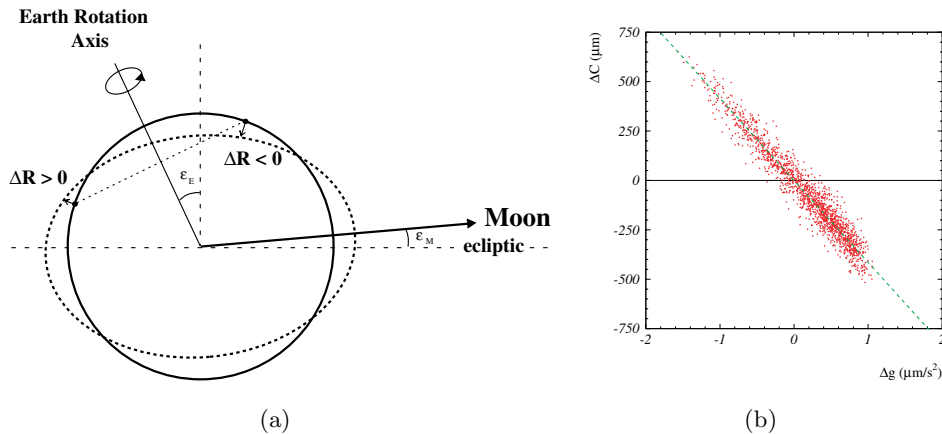


Figure 11: (a) Tidal deformation of the Earth surface due to the presence of the Moon. The inclination ϵ_E of the Earth rotational axis with respect to the plane of the ecliptic is 23.5° . The inclination ϵ_M of the lunar orbital plane is 5.1° . (b) Correlation between the change in circumference ΔC measured with the BOM system and the predicted tidal gravity correction Δg . The slope is $-410 \pm 20 \text{ s}^2$. Reference [18].

9 Vacuum chamber

- A. *The presented results on temperature distributions look promising. We are waiting for the final results with forced air.*
- B. *Because the inner tube is a critical component, one should consider protecting it with a layer (e.g. a Kapton foil) against possible scratches during sliding of the beam pipe or heating jacket. (The beam pipe, if containing Be, will probably also have a protective coating (?).)*

9.1 Results of bakeout tests

The tests performed up to now shows a perfect match with the calculated values. The insulation jacket used is 20 mm thick allowing a gap of 25 mm. The inner wall surface temperature is below 80 °C if the vacuum chamber is baked at 200 °C and below 90 °C if baked at 250 °C. The forced air will allow a reduction of this temperature. The heating power will always remain below 1500 W. Tests are on-going.

9.2 Protections of central tube and beam pipe

The vacuum chamber material is assumed to be an Aluminium-Beryllium alloy containing 62 % of the latter. This implies that strict safety rules must be followed⁹. A coating to the vacuum chamber external surface will be provided to ease its handling during the installation and avoid the corrosion of the highly reactive Be surface. Moreover, a polyimide foil attached permanently to the vacuum chamber external surface has been considered. This would prevent the vacuum chamber from scratching during the installation of the heating jackets. The tests performed with the mock-up have shown that this can be done in a smooth way.

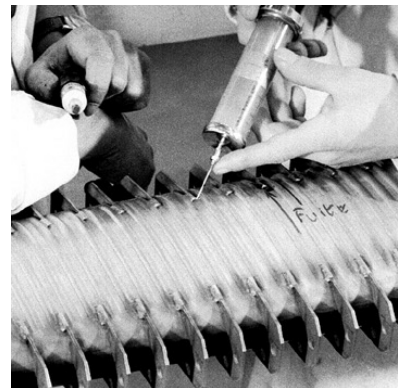
The inside surface of the central tube will be protected using Kapton sheet permanently bonded in position to avoid scratches during manipulation of the vacuum chamber and the associated bake-out equipment.

10 Assembly

- A. *It is not so clear to us what happens with the beam pipe. When does it come in? What implications on the scenario?*
- B. *A brief discussion of some relevant failure scenarios would also be useful, just to give a feeling on the consequences (in particular with respect to downtime and interference with nearby sub-systems).*

10.1 Vacuum chamber

The LHCb vacuum chamber installation scenario has not been fully studied. A preliminary study was launched in 2001 to settle a conceptual installation process. In what concerns the vacuum chamber through RICH 2, it will be inserted from the high Z-side with the RICH 2 already in place and pre-aligned. During this operation the tracking stations between the magnet and RICH 2, the calorimeters and the muon detectors must be in their open position. The vacuum chamber will be supported with wires in its high Z-side from the RICH 2. In the low Z-side it might be supported from the RICH 2 or from a dedicated frame. During the bake-out



⁹Safety Instruction IS N°25

operations, temporary supports will be installed.

10.2 Failure scenarios

Great care has been taken in the engineering of RICH2 to make an extremely simple and elegant structure which is robust and with as little radiation length added as possible. The crucial optics system is innovative whilst keeping it on a sound engineering level. We have also opted for a mirror alignment system which is not easily accessible after the closure of the detector. It does however not add unneeded material. It has also proven to be very reliable. The gas envelope is very light and do require high pass passive bubblers [7] to protect the volume from under or over pressure which could overstrain the central tube and the windows.

What would happen if



Figure 12: Large drift chamber after the implosion of the vacuum chamber. Courtesy of NA 48.

- Failure of the vacuum chamber.

An exchange of the vacuum chamber is reasonably fast. If it is due to an implosion in the vicinity of RICH2, it could have rather severe implications on the detector. See figure 12. A preliminary risk analysis have been carried out by the VELO group in collaboration with the vacuum group on the performance of this detector and its interface with the vacuum system [19]. There are only 2 identified undesired events that may cause the removal of the vacuum chamber. These are:

1. Leak from ambient air and failure of the protection systems.
2. Rupture of the LHCb VELO exit window or collapse of the beam pipe.

The estimated LHC downtime would be around 2 weeks. For the design of these items, the required maximum frequency for both of these events is set to $\sim 7 \cdot 10^{-4}$ /year. This corresponds to a $> 99.9\%$ probability to never to occur in 10 years.

- Realignment is required.

This can only be done during a long shut-down. At least one window will have to be removed which will require the vacuum chamber to be removed. The trackers and the calorimeters must be in an open position.

- Failure of window or central tube.

Small fractures could probably be repaired within one week without any down-time for the rest of the experiment. A replacement of any of these items could probably not be envisaged outside a long shut-down.

- Failure of a photon detector.
With some preparation, it could be replaced within a controlled access of about 5 hours.
- Failure of on-detector electronics.
Would be replaced within a controlled access of about 2 hours.

11 General remarks

- A. *Could one expect any corrosion of materials inside the gas volume due to radiation-induced chemical reactions?*
- B. *A short discussion would be useful on what would be the implications on the mechanical design in case of a change of choice for the photon detectors (HPD vs MAPMT).*
- C. *We asked what could be the effects on various metallic components due to a sudden switch-off of the magnet. But it was pointed out that the L/R of the magnet is of the order of 15 seconds.*

11.1 Corrosion

Free fluorine could be produced from a break-up of the CF_4 and Hydrofluoric Acid, HF, could be formed. HF reacts with glass, ceramics, and some metals. Reactions with metals may generate potentially explosive hydrogen gas. At 10 to 15 ppm, HF vapour is irritating to the eyes, skin, and respiratory tract. Further information about HF can be found in reference [20]. We aim to have the water level in the gas volume in the range of ≤ 100 ppm [7]. Precautions will also be taken in the gas system to detect any formation of HF.

Reference [21] discusses some CFX fluids as coolants at LHC. The samples were tested up to 30 kGy. The note gives the following conclusion:

- CF_3I is very radiation sensitive
- C_3F_8 , C_4F_{10} and C_6F_{14} have an acceptable activation level
 1. the highest expected dose induces less than 1 % radiolysis
 2. polymer deposit are formed over the tubing surface
 3. if present, the C-H groups are detrimental
 4. some radiolytic products may be reactive
 5. the online purification of the irradiated fluids are feasible

11.2 MAPMT as photon detector

The photon detector plane structure would be roughly the same. The basic unit is a matrix of 4×4 MAPMTs as described in reference [1]. A single quartz lens in front of each tube and a grid of Mumetal sheets will be made into one structure. As this is a rather complex structure it might lead to some relaxation of the layout constraint of the MAPMT pitch. The electronics would change. We are confident they could be arranged into a structure not much different from the current one. Cooling of the HV dividers would be necessary, but this is only a minor problem.

11.3 Emergency power failure of the magnet

The inductance of the magnet is in the range of 2 H. Given this value for the inductance, the time constant is about 16 seconds. Creation of eddy current in metallic components of the detector can therefore be neglected.

References

- [1] LHCb RICH Technical Design Report, CERN/LHCC 2000-0037, LHCb TDR 3, 7 September 2000.
- [2] LHCb RICH2 Engineering Design Review Report, LHCb EDR 2002-009
- [3] H. Ogren et al., Radiation tests on Transition Radiation Materials, February 29, 1996
- [4] Shirrell, C.D. and Halpin, J. , Moisture Absorption and Desorption in Epoxy Laminates, Composite Materials - Testing and Design - ASTM STP 617
- [5] Browning, C.E. et al. Moisture Effects in Epoxy Matrix Composites, ASTM STP 617
- [6] Sandorff, P.E. and Tajima, Y.A. , Moisture Distribution and Diffusivity in Composite Laminates, SAMPE Quarterly, January 1979.
- [7] M. Bosteels et al., LHCb RICH gas system proposal, LHCb-2000-079, 17 Apr 2001
- [8] D. Evans and R.P.Reed, The permeability of resin based composite materials to radiolytic gases, Cryogenics, 1998, Vol 38, Number 1 pp 149-154.
- [9] Vacuum Vademecum, LEYBOLD AG, Vacuum Technology
- [10] LHCb Muon System Technical Design Report, CERN/LHCC 2001-010, LHCb TDR 4, 28 May 2001
- [11] J.M. Juravlev et al., Investigation of power and spatial correlation characteristics of seismic vibrations in the CERN LEP tunnel for linear collider studies, CERN-SL/93-53 and CLIC-Note 217
- [12] K.Haga et al., THE VIBRATION MEASUREMENTS AT THE PHOTON FACTORY STORAGE RING BUILDING, Proceedings of EPAC 2000, Vienna, Austria.
- [13] E. Albrecht et al., Perfluorocarbon effects on composite and polymeric materials used within RICH detectors, DELPHI 95-21 RICH 66, 17 February 1995.
- [14] M. Tavlet, A. Fontaine and H. Schonbacher, Compilation of radiation damage test data. Part II, 2nd edition: Thermoset and thermoplastic resins, composite materials.
- [15] M. Alemi, Tecniche di rivelazione nei RICH di LHCb, PhD thesis, University of Milano, 1999.
- [16] T. Gys, Magnetic field simulations for the LHCb RICH2 detector, LHCb RICH 2002-029
- [17] Guy Wilkinson, Final energy calibration at LEP 1, CERN, Geneva, 20 April 1998.
- [18] J. Wenninger, Observation of Radial Ring Deformations using Closed Orbits at LEP, Proceedings of the 1999 Particle Accelerator Conference, New York, 1999
- [19] J.F.J. van den Brand et al., Preliminary Risk Analysis for the LHCb Vertex Detector, LHCb note 2001-079/VELO
- [20] NIST Standard Reference Database Number 69 - July 2001 Release
- [21] S. Ilie and M. Tavlet, Qualification of coolants and cooling pipes for future high-energy-particle detectors, CERN-TIS-2001-003-TE, February 2001.